Front. Mech. Eng. 2024, 19(5): 35
https://doi.org/10.1007/s11465-024-0805-3

RESEARCH ARTICLE

Model for atomization droplet size and energy distribution ratio at the distal end of an electrostatic nozzle

Dongzhou JIA[a,b], Keke JIANG[a], Yanbin ZHANG[c], Zhenlin LV[b], Changhe LI (✉)[c]

[a] *College of Mechanical Engineering and Automation, Liaoning University of Technology, Jinzhou 121001, China*
[b] *School of Materials Science and Engineering, Xi'an University of Technology, Xi'an 710048, China*
[c] *School of Mechanical and Automotive Engineering, Qingdao University of Technology, Qingdao 266520, China*
✉ *Corresponding author. Email: sy_lichanghe@163.com (Changhe LI)*

ABSTRACT Electrostatic atomization minimum quantity lubrication (EMQL) employs the synergistic effect of multiple physical fields to atomize minute quantities of lubricant. This innovative methodology is distinguished by its capacity to ameliorate the atomization attributes of the lubricant substantially, which subsequently augments the migratory and infiltration proficiency of the droplets within the complex and demanding milieu of the cutting zone. Compared with the traditional minimum quantity lubrication (MQL), the EMQL process is further complicated by the multiphysical field influences. The presence of multiple physical fields not only increases the complexity of the forces acting on the liquid film but also induces changes in the physical properties of the lubricant itself, thus making the analysis of atomization characteristics and energy distribution particularly challenging. To address this objective reality, the current study has conducted a meticulous measurement of the volume average diameter, size distribution span, and the percentage concentration of inhalable particles of the charged droplets at various intercept positions of the EMQL nozzle. A predictive model for the volume-averaged droplet size at the far end of the EMQL nozzle was established with the observed statistical value F of 825.2125, which indicates a high regression accuracy of the model. Furthermore, based on the changes in the potential energy of surface tension, the loss of kinetic energy of gas, and the electric field work at different nozzle orifice positions in the EMQL system, an energy distribution ratio model for EMQL was developed. The energy distribution ratio coefficients under operating conditions of 0.1 MPa air pressure and 0 to 40 kV voltage on the 20 mm cross-section ranged from 3.094‰ to 3.458‰, while all other operating conditions and cross-sections had energy distribution ratios below 2.06 ‰. This research is expected to act as a catalyst for the progression of EMQL by stimulating innovation in the sphere of precision manufacturing, providing theoretical foundations, and offering practical guidance for the further development of EMQL technology.

KEYWORDS atomization performance, EMQL, energy distribution, PIV observation, sustainable manufacturing

1 Introduction

Metalworking fluid, also known as cutting fluid, plays a very important role in the field of cutting. It mainly includes two categories: water solubility and oil solubility. To improve the lubrication, corrosion resistance, and rust resistance of cutting fluid, additives, such as extreme pressure agents, preservatives, and fungicides, should be included in the base fluid. However, these additives often contain harmful substances, such as chlorides, phosphates, nitrites, and sulfides [1,2]. These harmful substances exhibit poor degradation capabilities and can persist in the environment, thus causing adverse effects when released into soil and water sources. This persistence leads to eutrophication, red tide occurrences, and algal blooms in rivers, lakes, and oceans, which result in acute and subacute mortality in aquatic organisms. The extensive use of cutting fluids not only poses a threat to the environment and the health of operators but also incurs significant costs associated with post-treatment. Such practices are no longer aligned with the current principles of green, efficient, and sustainable development [3–5]. As an environmentally friendly machining technology, dry cutting eliminates the need for cutting fluids entirely. It addresses the issues related to the high

Received March 29, 2024; accepted May 8, 2024; online October 19, 2024

costs of cutting fluid usage and posttreatment, mitigates harm to the natural environment, and supports the health of operators. However, it presents challenges because of the absence of a cooling medium in the cutting zone. This absence severely restricts heat dissipation capacity, thus imposing stringent requirements on tool materials, workpiece materials, and process parameters. As such, dry cutting is not suitable for difficult-to-machine materials or operating conditions with high energy density [6–8].

With the rapid development of mechanical processing and manufacturing, issues such as environmental pollution and resource wastage have gained increasing prominence, thereby leading to a growing focus on green and sustainable processing methods. Minimum quantity lubrication (MQL) has emerged as an ideal alternative in this regard. This process is characterized by cleanliness, energy efficiency, and high reliability, thus making it a desirable substitute for traditional lubrication methods. MQL has found widespread application in metal cutting by offering advantages over conventional flood cooling and microlubrication techniques. It not only reduces usage costs and postprocessing requirements but also minimizes environmental and occupational hazards [9,10]. The effectiveness of MQL can be attributed to its unique delivery method wherein a small amount of microlubricant (10–100 mL/h) is atomized either within or outside the nozzle using compressed air (0.40–0.65 MPa). This atomization process forms a cluster of droplets that are carried by the airflow and directed toward the cutting zone, thus providing cooling and lubrication [11]. The increased specific surface area of atomized lubricant droplets significantly enhances their spreading and wetting properties. Consequently, even with a lubricant dosage as low as 5%, the performance achieved with MQL surpasses or equals that of traditional flood cooling methods. Consequently, researchers are actively exploring methods to improve the cooling and lubrication capabilities of MQL further by enhancing its atomization performance, specifically by reducing the average particle size and size distribution of the droplets. This area of research has garnered significant attention in the academic community [12].

The two separate processes that constitute nozzle atomization are the disintegration of small liquid clusters in the main jet region and the fragmentation of the continuous phase liquid at the nozzle exit in the initial jet region. At the nozzle outlet, the force, deformation, fracture, and fragmentation behavior of the continuous phase liquid are the main topics of discussion during the initial stage of atomization [13,14]. However, for practical applications of MQL, researchers are primarily concerned with the atomization process occurring in the main jet region. The main jet atomization is a continuous process without a fixed position or time scale for measurement. Specifically, it refers to a phenomenon wherein the small liquid clusters formed after the initial breakup at the nozzle exit enter the main jet region and undergo further continuous breakup or fragmentation under external forces [15,16]. Current research on the main jet atomization process primarily centers around the deformation and rupture processes of individual liquid clusters under external forces [17]. The findings demonstrate that the primary cause of breaking atomization is the velocity difference between small liquid and gas. Surface tension tends to contract the small liquid clusters into spherical shapes, while viscosity impedes their deformation. Only when the external forces exceed the internal forces can the liquid clusters undergo deformation or breakup [18]. Presently, high-speed imaging experiments and simulation methods are predominantly employed in the study of main jet atomization. Shlegel et al. [19] and Pham et al. [20] conducted experiments using high-speed camera particle image velocimetry (PIV) to capture the breakup process of small droplets on the main section of the jet; analyzed the effects of relative velocity, viscosity, and other factors on the breakup; and discussed the breakup mode under different Weber numbers. Ridolfi and Folgarait [21] and Wei et al. [22] simulated the surface waveforms of small liquid clusters and the process of their breakup into smaller droplets. They examined the influence of jet parameters on liquid deformation and breakup and predicted droplet size and distribution based on simulation results. However, the complex nature of the two-phase jet breakup process involves intense energy exchange between the gas and liquid phases; multiple force interactions; and direct and intricate influences of liquid morphology, external environment, and liquid properties on liquid atomization [23]. Furthermore, the main jet atomization process involves additional complexities, such as droplet collision, droplet coalescence, droplet evaporation, and droplet oscillation, thus further complicating the investigation of liquid atomization [24,25]. In light of practical industrial considerations, researchers have conducted extensive experimental studies on droplet breakup atomization using pneumatic nozzles by taking into account the characteristics of different atomizer types and statistical theories. They employ dimensionless parameters, such as the Weber number (We), Reynolds number (Re), and Mach number (Ma), to characterize the average droplet size resulting from droplet breakup, thereby developing various empirical and semiempirical models for predicting droplet size [26–28].

Based on the aforementioned studies, researchers have found that increasing the atomization gas pressure can effectively enhance atomization performance and the transport capability of microliquid droplets. However, this approach can have negative effects. In the process of liquid atomization and crushing, a violent energy exchange behavior emerges between the gas and liquid phases. At the same time, with the generation of a large number of fine oil mist particles, these particles may easily fly and disperse in the process of entering the cutting zone by relying on compressed gas [29,30]. Studies have shown that the oil mist droplets produced during the spraying process contain inhalable fine particles (PM_{10} and $PM_{2.5}$) with an average settling time of 8.2 s for PM_{10} particles and over 1.5 h for $PM_{2.5}$ particles. When the concentration of suspended particles in the air exceeds a certain level, it can severely impact respiratory system's health. These fine particles deposit in organs, such as the respiratory tract, alveoli, and bronchi, which leads to allergies, pneumonia, irritant reactions, asthma, pulmonary emphysema, and even various types of cancer, including laryngeal cancer, thus posing a serious threat to human health [31–33]. Therefore, good atomization performance and green processing requirements are difficult to take into account by using pneumatic atomization. Hence, Jia et al. [34] proposed an electrostatic atomization-assisted grinding technology for MQL in 2017. The inspiration for this technology stems from the fact that electrostatic atomization technology exhibits small atomization particle size, high uniformity, and strong enveloping ability. Moreover, it has demonstrated significant advantages over other atomization methods in various fields, including the preparation of nanoparticles, nanocapsules, nanofibers, and high-performance batteries in the bio-based materials and pharmaceutical sectors [35–37]. Furthermore, research in areas such as water coal slurry atomization, liquid fuel atomization, and electrostatic spraying has shown that charged liquid atomization can significantly refine droplet size and reduce the range of droplet size distribution [38,39]. Subsequently, Lv et al. [40] and other researchers [41–48] conducted experiments on electrostatic atomization in the context of MQL cutting for various metal materials. The results of the experiment demonstrated a significant improvement in tool life and workpiece surface quality.

Compared with the traditional MQL, under the action of multiple physical fields, the force of the liquid film is more complicated, and the physical properties of the lubricant itself are changed. Thus, examining the atomization characteristics and calculating the energy distribution are particularly difficult. Therefore, the droplet size generated during the atomization process of charged small liquid clusters must be analyzed statistically, and relevant prediction models must be established to guide the application in this field. Meanwhile, in the introduction of the external electric field, no comprehensive study has been conducted on the energy consumption of the atomization system. Although researchers have done some research work on energy dissipation and energy transfer in the process of electrostatic atomization, no relatively complete energy distribution model has been developed so far. Therefore, this study focuses on the atomization process in the primary jet section of an internal-mixing two-phase flow nozzle. Laser particle analyzers are utilized to measure the volume mean diameter, size distribution span, and inhalable particle concentration at different cross-sectional positions along the primary jet section. Furthermore, based on a dimensionless analysis, a predictive model for the volume mean diameter is established, which correlates directly with the effective Weber number, electric Euler number, void fraction, and the ratio of jet length to nozzle diameter. The study investigates the variations in the potential energy of surface tension, the loss of kinetic energy of gas, and electric field work at different jet positions. Additionally, an energy distribution ratio model for the atomization system is developed based on the relationship among these factors. The influence of various jet parameters, especially gas velocity and initial voltage, on energy distribution is analyzed. The results of this study not only stimulate further understanding of energy distribution behavior during the atomization process but also provide practical guidance for the precise and controllable application of the average droplet size in industrial settings [49–52].

2 Experimental investigation of the breakup and atomization of charged small liquid clusters

2.1 Experimental setup

Figure 1 presents the experimental setup for investigating small cluster breakup and the particle size of atomization under the electrostatic atomization minimum quantity lubrication (EMQL) conditions, as well as the construction of the energy distribution ratio model. The electrostatic atomization system comprises the Bluebe microlubrication system, Hongda high-voltage DC power supply, gas/liquid supply system, and internally mixed two-phase flow electrostatic nozzle (self-made). The gas pressure can be adjusted continuously within the range of 0–0.8 MPa, while the liquid flow rate can be adjusted continuously within the range of 0–200 mL/h. The high-voltage DC power supply allows for the continuous adjustment of the voltage between 20 and 60 kV. The nozzle outlet radius, which is denoted as r_0, is set to 1×10^{-3} m. Faraday cages and picoammeters are employed to measure the charge-to-mass ratio of atomized droplets. The Winner319 laser particle analyzer is utilized to measure the average droplet size and its distribution. A vortex flowmeter is used to measure the gas flow rate at the nozzle outlet. The i-SPEED 221 high-speed camera and LED high-intensity light source are employed to observe the liquid film evolution at the nozzle outlet visually and extract information for calculating the initial liquid velocity.

2.2 Experimental design

Soybean oil, which is primarily composed of fatty acids,

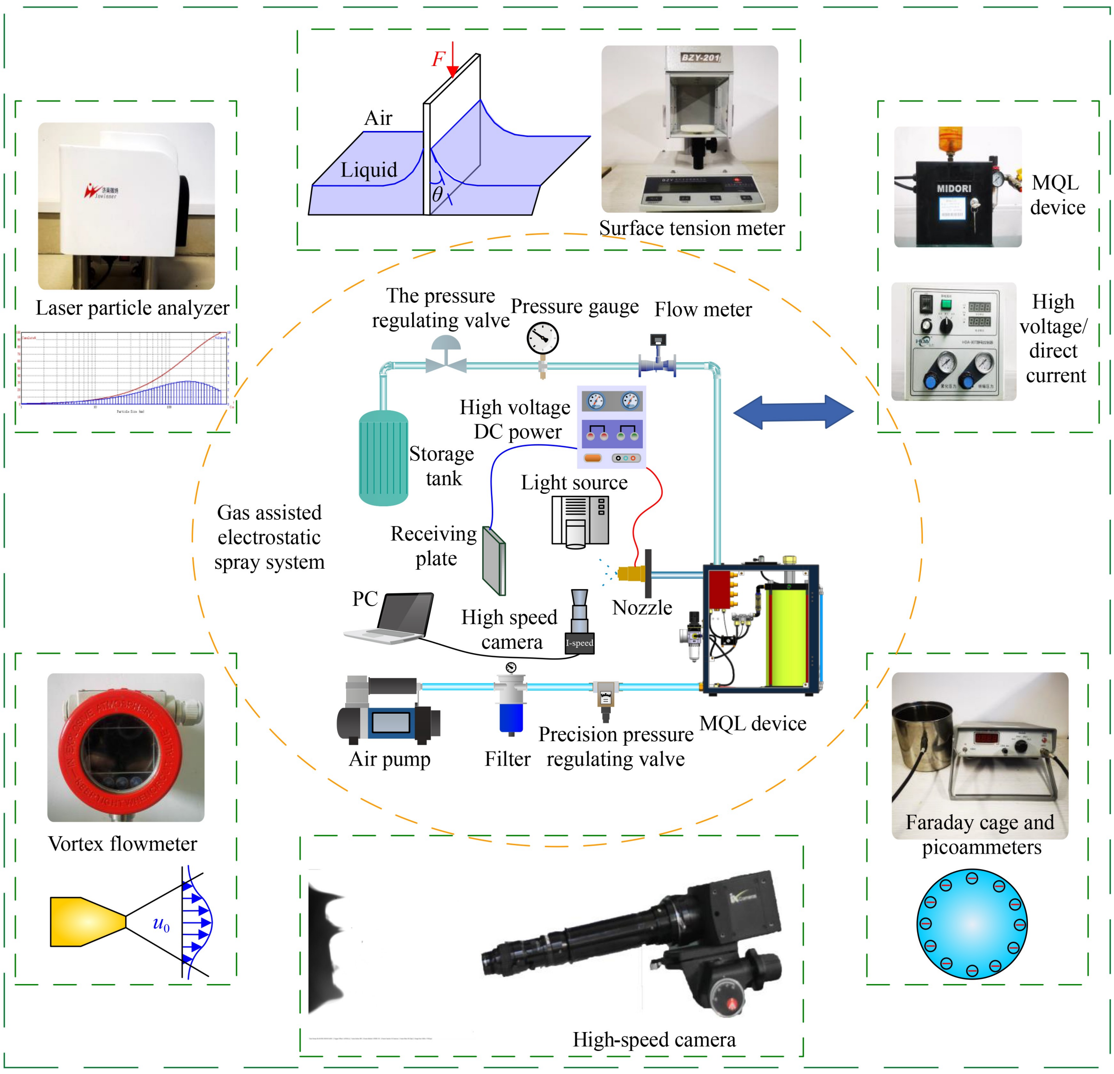

Fig. 1 Experimental and measuring equipment.

contains polar functional groups, such as –COOH and –COOR. These groups form a physically adsorbed film via Van der Waals forces along metal surface molecules, thereby facilitating lubrication and friction reduction. Additionally, soybean oil undergoes metal saponification reactions with metal surfaces, which result in the formation of chemically adsorbed films that also contribute to lubrication and friction reduction. Consequently, soybean oil is selected as the atomized oil, and the flow rate is fixed at 60 mL/h. A pulse-type liquid supply with a duty ratio of 1:5 is employed. The distance between the electrostatic nozzle and the receiving plate is set to 50 mm. A full factorial experiment is conducted using voltage, air pressure, and spray distance as independent variables. The voltage levels are selected as 0, 20, 25, 30, 35, and 40 kV, while the air pressure levels are set at 0.1, 0.2, 0.3, and 0.4 MPa. In the case of free jet injection, an initial jet length that is approximately 6.4 times the nozzle diameter exists within which the primary atomization of the liquid occurs.

As shown in Fig. 2, regarding the initial atomization behavior at the outlet of the EMQL nozzle, we have developed a mathematical model for the volume-averaged droplet size during the initial atomization process based on fluctuation theory. This model sheds light on the near-field atomization mechanism of the EMQL nozzle. Our analysis reveals the significant influence of the applied external electric field on the morphology of the lubricant annular film at the nozzle outlet. As shown in Figs. 2(a) and 2(b), the annular film morphology under the pure electric field condition of 40 kV exhibits the formation of the distinctive Taylor cone and the presence of monodisperse small droplets. Figure 2(c) presents the annular film morphology under the pure pneumatic condition of 0.2 MPa, which is characterized by minimal film oscillation and a relatively lower number of wave modes. Meanwhile, Fig. 2(d) shows the annular film morphology under the condition of 0.2 MPa and 30 kV, where the transverse oscillation of the film becomes increasingly pronounced, accompanied by a growing number of wave

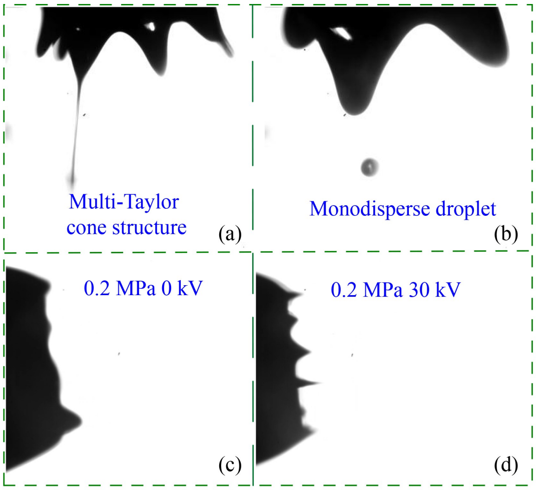

Fig. 2 Nozzle liquid film characteristics.

modes, shortened wavelengths, and a more uniform distribution between wave peaks [1]. Considering that the actual working position of the MQL processing nozzle is not proximal to the nozzle itself, this study further investigates the atomization characteristics in the spray zone at distances of 20, 30, 40, and 50 mm. By employing a laser particle size analyzer, we measure the volume-averaged droplet size under different voltage and air pressure conditions across various spray cross-sections while simultaneously tracking the distribution pattern of droplet sizes and the content of PM_{10} and $PM_{2.5}$ particles.

2.3 Measurement results and analysis of particle size

As shown in Fig. 3, the volume average diameter of droplets (VAD) under different voltage and air pressure conditions is experimentally measured. The observed variations in the VAD on different cross-sections, which are measured at various distances from the nozzle outlet, exhibit a consistent trend.

As shown in Fig. 3, the average volume particle size of the droplets decreases consistently with increasing voltage and air pressure. Moreover, for a given air pressure and voltage, an increase in spray distance results in a decreasing trend in the average volume particle size of the subdroplets. Notably, this behavior differs in the case of an air pressure of 0.1 MPa and voltage of 0 kV. Analysis reveals that at an air pressure of 0.1 MPa, the gas atomization capability is insufficient, thus leading to droplet breakup at 20 and 30 mm. However, as the gas kinetic energy dissipates rapidly, the atomization capability no longer supports further breakup of the liquid at 40 mm. Instead, droplet collision and coalescence occur, thus resulting in an increase in the average volume particle size. However, when the nozzle is charged, the decrease of the surface tension of the liquid itself and the effect of the electric field force do not appear in this phenomenon. Under the action of the electric field, the same charge accumulates on the surface of the droplet and causes the skin phenomenon. The charge repulsion helps to offset the surface tension, and the droplet is more likely to break [1]. Additionally, droplet collision and coalescence are effectively avoided because of the repulsive forces between droplets carrying the same charge. With increasing voltage and air pressure, the average particle size of droplet volume continuously decreases. Under identical air pressure and voltage conditions, the average particle size of the subdroplet volume decreases with increasing spray distance, thus indicating a consistent effect of the electric field on particle size reduction at different positions. At a voltage of 30 kV, the droplet size decreases rapidly with increasing air pressure. This decreasing trend becomes pronounced with the increasing distance, which suggests that the influence of the airflow field in promoting particle size reduction gradually strengthens at different positions. Notably, the most significant reduction in particle size occurs during the transition from an air pressure of 0.1 to 0.2 MPa, thereby emphasizing the inadequate atomization capability at 0.1 MPa air pressure.

2.4 Span assessment of droplet size distribution at the far end of the nozzle

To investigate the impact of aerodynamic and electrical parameters on the particle size distribution and the generation of fine droplet concentration during the spraying process at different spray distances, we have collected data on the volume-averaged particle size of the droplet population, span values (R.S) of the particle size distribution, and the percentage content of $PM_{10}/PM_{2.5}$ under varying voltage and air pressure conditions. Figure 4 shows the cumulative distribution curves of droplet sizes for different voltage conditions at 0.3 MPa/30 mm, various air pressure conditions at 30 kV/30 mm, and different spray distance conditions at 0.3 MPa/30 kV.

The droplet size distribution span, which is represented by the R.S value, exhibits a decreasing trend with increasing voltage. Under conditions of 0.3 MPa/30 mm, compared with pure pneumatic atomization, the droplet size distribution span decreases by 47.85% at a voltage of 40 kV. Furthermore, the R.S value of the droplet size distribution span gradually rises with increasing air pressure. At 30 kV/30 mm, compared with 0.1 MPa, the droplet size distribution span increases by 159.14% at an air pressure of 0.4 MPa. However, the R.S value of the droplet size distribution span shows little sensitivity to changes in spray distance. Under conditions of 0.3 MPa/30 kV, with increasing spray distance, the distribution span initially increases and then decreases until it reaches its maximum at 30 mm. Notably, under various spray distance conditions, the variation in droplet distribution span is minimal with a maximum difference of only 0.031.

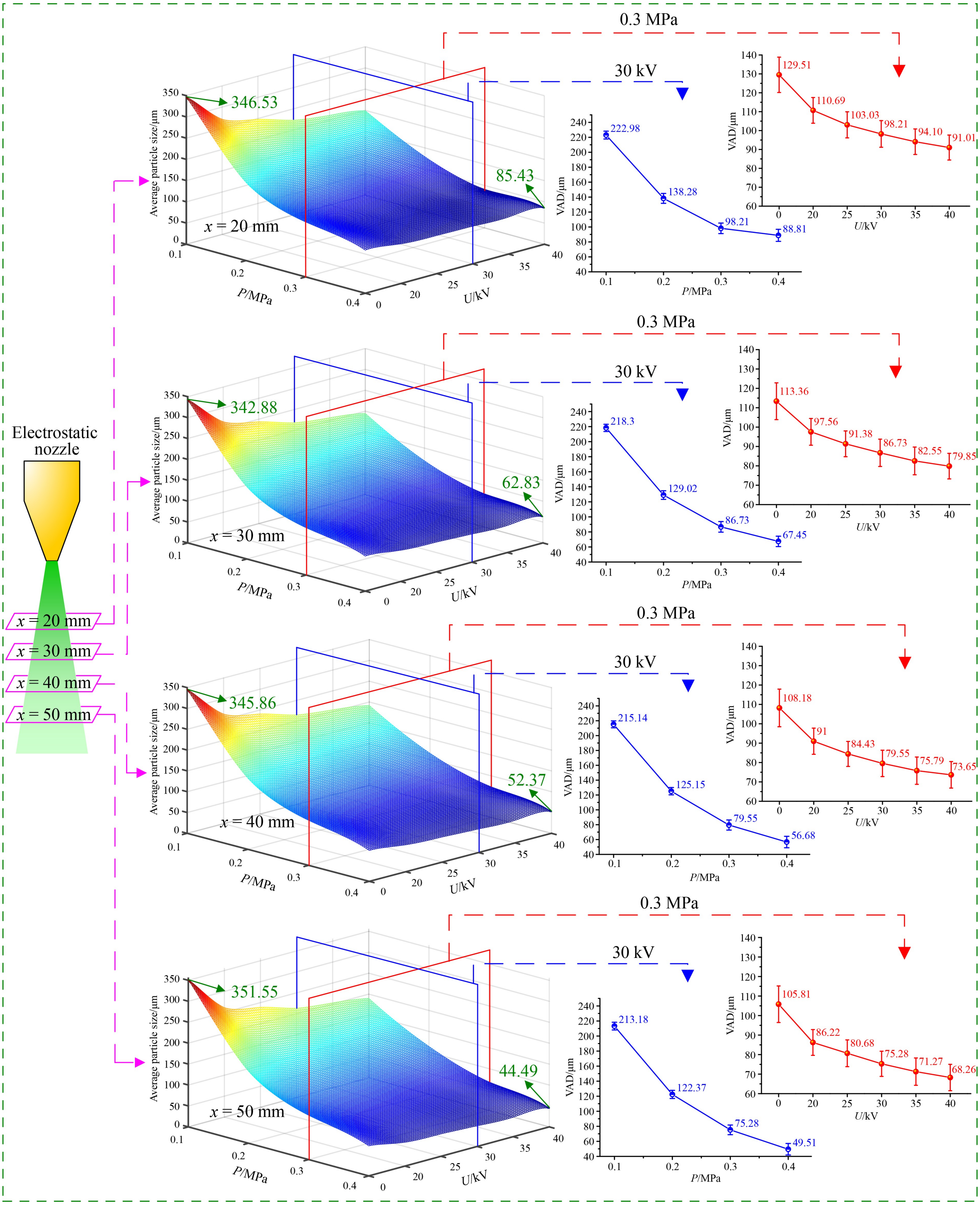

Fig. 3 Average particle size of droplet under different working conditions.

2.5 Percentage concentration assessment of PM_{10} and $PM_{2.5}$ at the far end of nozzle

Given the poor atomization ability when the gas pressure is 0.1 MPa, the droplet size is larger, thus resulting in the practical absence of small droplets contributing to the generation of PM_{10} and $PM_{2.5}$. Therefore, the subsequent discussion does not include the analysis of PM_{10} and $PM_{2.5}$ levels under such conditions. As shown in Fig. 5, the percentage concentration of PM_{10} at the cross-sections of 20, 30, 40, and 50 mm spray distances under various air pressure and voltage conditions.

Taking the 20 mm spray distance section as an example, the percentage concentration of PM_{10} significantly

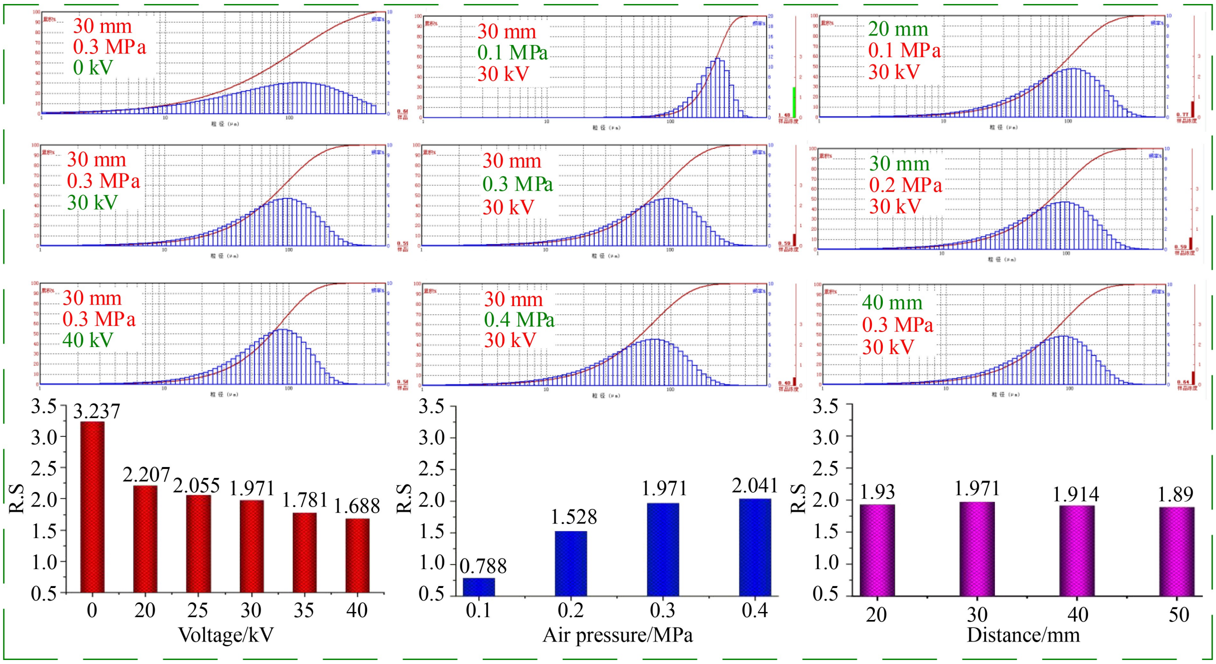

Fig. 4 Droplet size distribution under various conditions. R.S: span values.

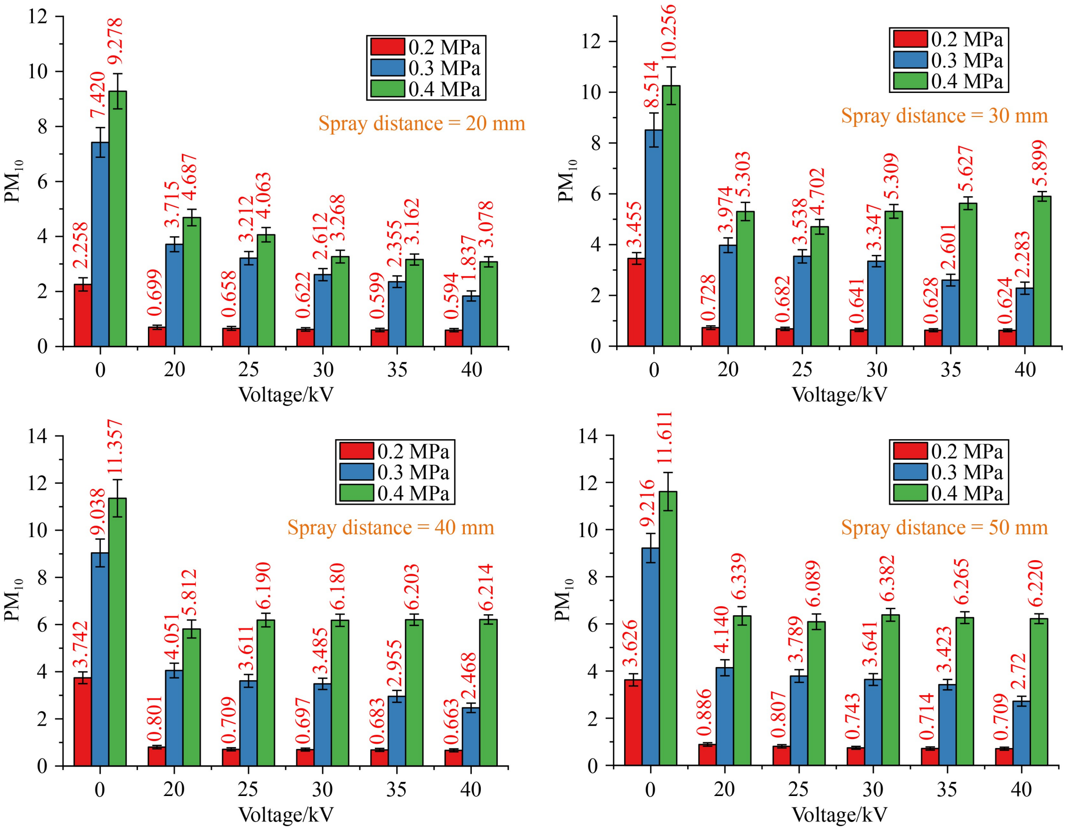

Fig. 5 Percentage concentration of PM$_{10}$ at different spray distances.

increases under nonelectrified conditions with increasing air pressure. The maximum increase is observed at 228% when the air pressure is raised from 0.2 to 0.3 MPa. This phenomenon is attributed to the accelerated fragmentation and atomization of small liquid clusters within this pressure range. The intensified interaction between the gas and droplets at higher air pressure shifts the fragmentation process toward an explosive mode, thus resulting in an increased production of smaller droplets. However, when the air pressure is further increased from 0.3 to 0.4 MPa, the rate of increase in the percentage concentration of PM_{10} diminishes to 25.14%. This saturation effect occurs because the liquid fragmentation process reaches a near-saturation state at an air pressure of 0.3 MPa, thereby making the effect of further increasing the gas pressure less noticeable. Comparatively, the impact of voltage on the percentage concentration of PM_{10} under identical air pressure conditions reveals that charging the liquid effectively suppresses the formation of small droplets in the PM_{10} range. This suppression is primarily attributed to the low generation of small droplets during the initial atomization stage under charged conditions. For example, in the case of the 20 mm/30 kV configuration, the percentage concentration of PM_{10} decreases by 72.45%, 64.8%, and 64.78% at air pressures of 0.2, 0.3, and 0.4 MPa, respectively, compared with nonelectrified conditions. The greater reduction in concentration observed at 0.2 MPa can be attributed to the smaller base value used in the calculations. A comparison of different spray distance conditions shows that when the air pressure is either 0.2 or 0.3 MPa, the influence of voltage on PM_{10} is more evident; that is, the suppression effect continues to increase with the increase of voltage. However, this relationship no longer holds true when the air pressure reaches 0.4 MPa. This outcome can be attributed to the excessively vigorous interaction between the gas and liquid phases at an air pressure of 0.4 MPa, which increases atomization randomness. This observation indicates that higher air pressures are not conducive to the controlled parameterization of atomization. Using the 30 kV/0.3 MPa condition as an example, the analysis of the percentage concentration of PM_{10} at different spray distance sections reveals a distinct variation when transitioning from 20 to 30 mm with a small degree of change as the distance further increases. Notably, the concentration measured at 40 mm is lower than that at 30 mm. This discrepancy arises from the fact that the particle size measurements are not obtained within the same atomization process but represent an average of multiple measurements, thus introducing a certain degree of numerical fluctuation.

Figure 6 presents the percentage concentration of $PM_{2.5}$ at the cross-sections of 20, 30, 40, and 50 mm spray distances under different air pressure and voltage conditions.

The percentage concentration of $PM_{2.5}$ closely resembles that of PM_{10} under different conditions with differences primarily in magnitude. Increasing the gas pressure under nonelectrified conditions significantly

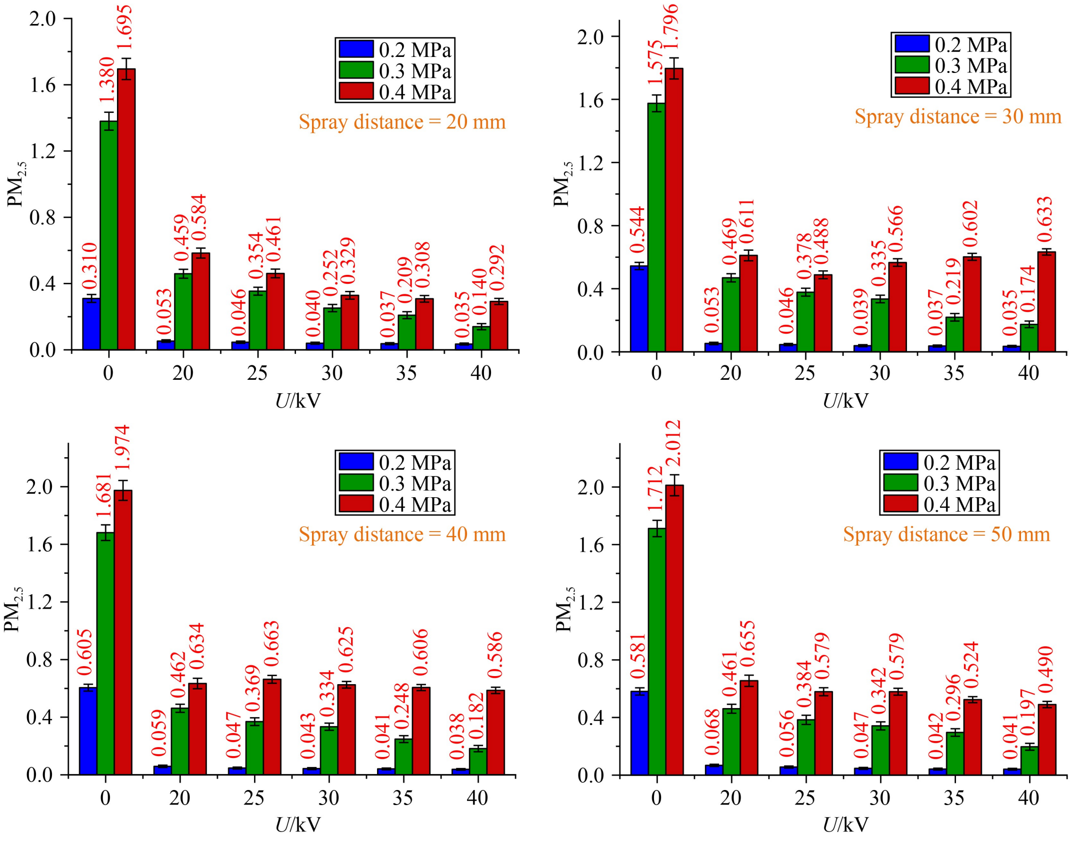

Fig. 6 Percentage concentration of $PM_{2.5}$ at different spray distances.

enhances the percentage concentration of $PM_{2.5}$. The maximum value of 2.012% is observed at a spray distance of 50 mm and an air pressure of 0.4 MPa. Electrifying the liquid effectively reduces the generation of small droplets in the $PM_{2.5}$ range. High voltages result in a pronounced suppression effect at 0.2 and 0.3 MPa, while the impact of voltage on $PM_{2.5}$ generation is enhanced at 0.4 MPa but not significantly, following a similar trend observed for PM_{10} concentration. Furthermore, the influence of spray distance on the percentage concentration of $PM_{2.5}$ is relatively minor.

3 Mathematical model of breakup and atomization droplet size for small liquid clusters

3.1 Development of a mathematical model for the size distribution of fragmented and atomized droplets

The Buckingham Pi Theorem, also known as the π theorem, is a universal method of dimensional analysis that establishes relationships between various parameters and the governing parameters based on experimental observations. By constructing dimensionless groups and analyzing their physical interpretations, a correspondence is established between dimensionless groups and the target phenomenon. For a complex physical process described by n variables, including m fundamental dimensions, the phenomenon can be expressed using $n-m$ independent dimensionless groups.

Based on the particle size experiments and energy distribution coefficients of the gas-assisted EMQL spraying system mentioned above, several observations can be made. The VAD decreases with increasing nozzle exit gas velocity (u_0), increasing nozzle voltage (U_0), and increasing spray distance (x). The analysis of electrostatic effects suggests that electrostatics can alter the liquid's surface tension coefficient, thus implying a proportionate relationship between the surface tension coefficient (σ^*) and VAD. Additionally, VAD is correlated with the liquid film thickness, which can be represented by the gas core radius (r_g) and reflect the gas-to-liquid flow rate ratio of the atomization system. Although this study does not specifically discuss the comparison of nozzle exit diameters (d_0), numerous studies have shown that the average droplet size increases with an increase in the nozzle exit diameter, thereby indicating a proportional relationship between VAD and d_0. To clarify the physical meanings of the dimensionless groups involved in the theory, the relative permittivity (ε_r) and gas density (ρ_g) are introduced. According to the Buckingham Pi Theorem, the aforementioned physical quantities can be expressed as follows:

$$f(\mathrm{VAD}, u_0, U_0, \varepsilon_r, \rho_g, d_0, r_g, \sigma^*, x) = 0. \tag{1}$$

The equation comprises nine physical quantities, namely, ε_r with dimensions $[L^{-3}M^{-1}T^4I^2]$, U_0 with dimensions $[L^2MT^{-3}I^{-1}]$, u_0 with dimensions $[LT^{-1}]$, ρ_g with dimensions $[ML^{-3}]$, d_0 with dimension [L], r_g with dimension [L], σ^* with dimensions $[MT^{-2}]$, x with dimension [L], and VAD with dimension [L]. These quantities involve four fundamental dimensions, namely, M (mass), L (length), T (time), and I (current). Consequently, the equation can be reformulated in terms of five dimensionless groups as follows:

$$f_1(\pi_1\pi_2\pi_3\pi_4\pi_5) = 0. \tag{2}$$

By selecting d_0, u_0, U_0, and ρ_g as repeating variables, each dimensionless group can be expressed using the repeating variables and one nonrepeating variable in the following manner:

$$\pi_1 = d_0^{a1}, U_0^{a2}, u_0^{a3}, \rho_g^{a4}, \mathrm{VAD}, \tag{3}$$

$$\pi_2 = d_0^{a1}, U_0^{a2}, u_0^{a3}, \rho_g^{a4}, \varepsilon_r, \tag{4}$$

$$\pi_3 = d_0^{a1}, U_0^{a2}, u_0^{a3}, \rho_g^{a4}, r_g, \tag{5}$$

$$\pi_4 = d_0^{a1}, U_0^{a2}, u_0^{a3}, \rho_g^{a4}, \sigma^*, \tag{6}$$

$$\pi_5 = d_0^{a1}, U_0^{a2}, u_0^{a3}, \rho_g^{a4}, x. \tag{7}$$

Taking π_1 as an example, dimensional normalization calculation is

$$M_0L_0T_0I_0 = (L)^{a1}(L^2MT^{-3}I^{-1})^{a3}(ML^{-3})^{a1}L. \tag{8}$$

Equating the dimensional exponents on both sides of the equation, the following is obtained: $a_1 = -1$, $a_2 = 0$, $a_3 = 0$, and $a_4 = 0$. Note that $\pi_1 = \mathrm{VAD}/d_0$. Similarly, $\pi_2 = \varepsilon_r U_0^2/\rho_g u_0^2 d_0^2$. The electric Euler number E_U is $\pi_3 = r_g/d_0$, and its physical significance is consistent with the void fraction α. Therefore, it can be expressed in terms of the void fraction α, π_4 ($\pi_4 = \rho_g u_0^2 d_0/\sigma^*$), the Weber number, π_5 ($\pi_5 = d_0/x$), and nozzle diameter to jet length ratio F_s. The function relationships among the dimensionless groups can be established as follows:

$$\frac{\mathrm{VAD}}{d_0} = A\left(\frac{\rho_g u_0^2 d_0}{\sigma^*}\right)^B \left(\frac{\varepsilon_r U_0^2}{\rho_g u_0^2 d_0^2}\right)^C (\alpha)^D \left(\frac{d_0}{x}\right)^E, \tag{9}$$

where A is the nozzle structure coefficient; and B, C, D, and E are the fitting exponents for the corresponding physical quantities. Taking the logarithm of both sides of the equation yields the following:

$$\ln\left(\frac{\mathrm{VAD}}{d_0}\right) = \ln A + B\ln\left(\frac{\rho_g u_0^2 d_0}{\sigma^*}\right) + C\ln\left(\frac{\varepsilon_r U_0^2}{\rho_g u_0^2 d_0^2}\right) + D\ln\alpha + E\ln\left(\frac{d_0}{x}\right). \tag{10}$$

Combined with the experimental data of the volume-averaged droplet diameter obtained under various operating conditions, the fitting coefficients can be determined through the least squares. Given the presence of voltage in the numerator of the electric Euler number, taking the logarithm is not meaningful when the voltage is zero. Therefore, this empirical formula is only applicable to charged operating conditions and does not consider noncharged conditions. The correlation of the experimental volume-averaged droplet diameter VAD is as follows:

$$\frac{\mathrm{VAD}}{d_0} = 0.3852\left(\frac{\rho_{\mathrm{g}} u_0^2 d_0}{\sigma^*}\right)^{-0.4850} \cdot \left(\frac{\varepsilon_{\mathrm{r}} U_0^2}{\rho_{\mathrm{g}} u_0^2 d_0^2}\right)^{0.0036} \cdot \alpha^{-10.1710} \cdot \left(\frac{d_0}{x}\right)^{0.2568}. \tag{11}$$

Equation (11) demonstrates that the volume-averaged droplet diameter exhibits an inverse correlation with the Weber number, thus indicating that larger Weber numbers correspond to smaller droplet sizes. The Weber is positively correlated with the initial gas velocity and negatively correlated with the liquid surface tension coefficient. Therefore, increasing the gas velocity or decreasing the liquid surface tension coefficient will result in a reduction in the volume-averaged droplet diameter. Notably, although the experiment shows that the droplet size decreases with the increase of voltage, the electric Euler number contains the initial gas velocity term, which is inversely proportional to the electric Euler number. By considering the combined effects of the electric field and the airflow field, we find that the droplet average diameter is directly proportional to the electric Euler number. This observation implies that larger electric Euler numbers correspond to larger droplet sizes. The void fraction, which is mostly dictated by the gas core radius of the annular liquid film at the electrostatic nozzle outlet, is inversely proportional to the volume-averaged droplet size, which also illustrates that the droplet size is influenced by the thickness of the liquid film. A larger gas nucleation radius, which is associated with a higher gas velocity, leads to a larger gas void fraction. Additionally, the droplet average diameter is positively correlated with the ratio of the nozzle diameter to jet length, but decreases as the spray distance increases. The influence weights of various dimensionless physical quantities on the average droplet size in atomization can be determined based on their respective exponent magnitudes. The void fraction has the greatest impact weight, while the electric Euler number has the smallest impact weight. The Weber number and the electric Euler number take into account the synergistic effects of the airflow field and the electric field. However, the analysis suggests that the airflow field has a greater influence on the droplet average diameter.

3.2 Validation of the droplet size model

The coefficient of determination, R^2, is a crucial metric for assessing the goodness of fit in a regression model. It represents the ratio of the sum of squares of regression to the sum of squares of total deviation, typically ranging from 0 to 1. In the fitted model, the R^2 value is calculated as 0.9778, which indicates a high level of significance. Furthermore, the F-statistic for this model is 825.2125, which significantly surpasses the critical F-value. The test P-value is 0, which is less than the default value of 0.05, thus further confirming the high accuracy of the model regression. These statistical indicators collectively demonstrate a significant relationship between the average droplet size and the Weber number, electric Euler number, void fraction, nozzle diameter, and jet length ratio.

To assess the model's performance visually, Fig. 7 presents the residual plot at a confidence level of 95%. Based on a sample size of 80, all the observed data points are evenly distributed around a zero point, and the confidence intervals of the residuals encompass a zero point within their ranges. The residual plot exhibits a reasonably normal distribution pattern. It shows that the regression equation can better conform to the original data of the average particle size of the droplet volume.

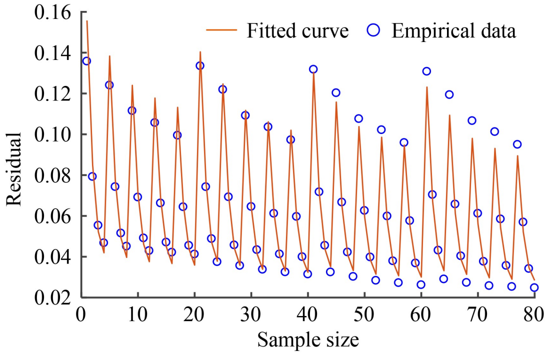

Fig. 7 Diagram of residual lever.

To show the experimental discrete data points and the fitting accuracy of the empirical formula of the Buckingham Pi Theorem intuitively, Fig. 8 presents the relationship between the experimental and theoretical data. The analysis shows random errors in the measurement of nozzle outlet gas velocity, charge-to-mass ratio, detection position, and nozzle outlet liquid film velocity. In addition, the measurement error of the laser particle size analyzer leads to some errors in the empirical formula, and the error is within the acceptable range. Therefore, the utilization of this empirical formula enables the prediction of the volume-averaged droplet diameter in gas-assisted electrostatic spraying systems at varying spray distances. This outcome provides a theoretical and experimental foundation for the controlled application of average droplet sizes in electrostatic spraying engineering.

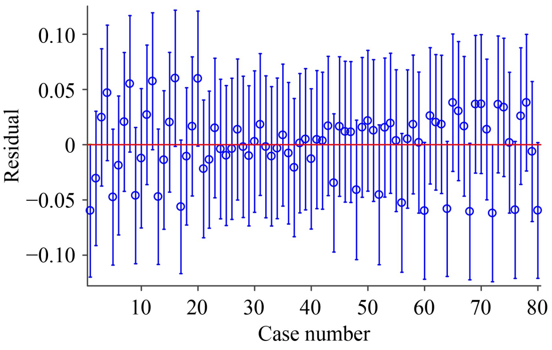

Fig. 8 Fitting degree of particle size formula of broken atomized droplets.

4 Model for energy distribution ratio in atomization systems

The atomization behavior of the liquid in the main section of the jet includes the violent energy exchange process between the liquid phase and the gas phase. Moreover, it demonstrates the effect of the electric field on the droplet. The atomization efficiency is typically used to characterize the relationship between the energy input of the atomization system and the size of the generated droplets. The change of the droplet size in the energy range is characterized by the change in the surface tension potential energy of the (ΔW_S) of the droplet system during the atomization process. In gas-assisted electrostatic atomization systems, the input energy primarily consists of the kinetic energy of gas and the potential energy of the electric field. A vigorous energy exchange occurs between the high-speed gas formed by jet and the liquid droplets and the surrounding air. The loss of kinetic energy of gas (ΔK) primarily arises from friction with the surrounding gas, the exchange of kinetic energy between the gas and liquid phases, and the promotion of liquid deformation. As such, this process is highly complex. Additionally, the electric field force in the atomization process performs work on the charged liquid droplets as an external force. The ratio T, which is defined as the ratio of the ΔW_S following liquid fragmentation to the sum of the ΔK and the work done by the electric field (ΔW_E), quantifies the proportion of system energy converted into liquid surface tension during the atomization process. This ratio T serves to characterize the atomization efficiency of the system.

$$T = \frac{\Delta W_\mathrm{S}}{\Delta K + \Delta W_\mathrm{E}}. \tag{12}$$

4.1 Change in the potential energy of surface tension in atomization systems

Under the condition of pneumatic atomization, the liquid atomization process is assumed to be completed by a split, thus ignoring the intermediate change process. In other words, a mother droplet with a radius of R is assumed to split into n daughter droplets, each with a radius of r. The number of daughter droplets n can be expressed based on the principle of equal volumes as follows:

$$n = R^3/r^3. \tag{13}$$

The surface potential energy (W_S1) of the mother droplet before fragmentation is

$$W_\mathrm{S1} = 4\pi\sigma R^2, \tag{14}$$

where σ (N/m) represents the surface tension coefficient of the liquid phase.

The total surface potential energy (W_S2) of the group of daughter droplets formed after the fragmentation of the liquid is given by

$$W_\mathrm{S2} = \frac{4\pi\sigma R^3}{r}. \tag{15}$$

Therefore, the change in surface potential energy (ΔW_S) of the liquid before and after fragmentation is given by

$$\Delta W_\mathrm{S} = W_\mathrm{S2} - W_\mathrm{S1} = \frac{4\pi\sigma R^2(R-r)}{r}. \tag{16}$$

In this experiment, soybean oil, which is a dielectric material, is used as an atomizing oil. The surface tension of soybean oil at room temperature is 32.17 mN/m. In general, the surface tension of soybean oil decreases with the increase of voltage under the same gas pressure condition. Neglecting the influence of gravity, the droplet tends to shrink into an ideal sphere with a radius of R under the action of surface tension. This contraction results in the presence of static pressure, P_s inside and outside the droplet, as shown in Fig. 9(a). When a droplet acquires a charge, the charges primarily accumulate on its surface because of the skin effect, thus allowing for a simplification into a surface charge model. Under the repulsive force exerted by like charges on the surface, the droplet experiences an opposing electrostatic expansion force, P_e, as illustrated in Fig. 9(b) [1].

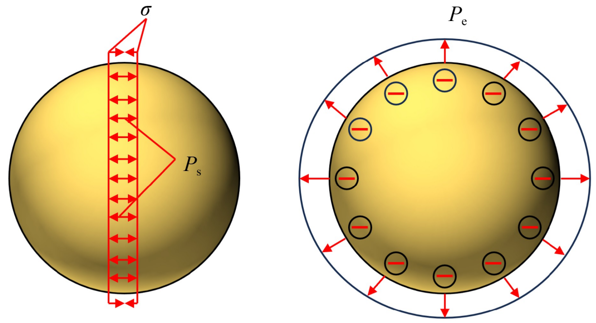

Fig. 9 Force analysis of charged droplet. The left diagram shows the hydrostatic pressure. The right diagram shows the electrostatic expansion pressure.

The charged droplet is assumed to be an ideal sphere, and its surface does not fluctuate. The total charge carried by the droplet is Q_d (C), which is uniformly distributed on the outer surface of the droplet. According to the superposition of electrostatic fields, the electric field strength E_s at any distance r_s from the center of the droplet can be calculated as follows [52]:

$$E_\mathrm{s}=\frac{Q_\mathrm{d}}{4\pi\varepsilon_\mathrm{r}\varepsilon_0 r_\mathrm{s}^2}, \tag{17}$$

where r_s (m) is the distance from the calculated point to the center of the sphere. E_s (V/m) is the electric field intensity from the center of the sphere to the point r_s.

The surface potential of the spherical droplet and the electrostatic energy stored in the droplet are further obtained as follows:

$$U_\mathrm{d}=\int_R^\infty E_\mathrm{s}\mathrm{d}r_\mathrm{s}=\frac{Q_\mathrm{d}}{4\pi\varepsilon_\mathrm{r}\varepsilon_0 R}, \tag{18}$$

$$W_\mathrm{e}=\int_0^{Q_\mathrm{d}} U_\mathrm{d}\mathrm{d}Q_\mathrm{d}=\frac{Q_\mathrm{d}^2}{8\pi\varepsilon_\mathrm{r}\varepsilon_0 R}, \tag{19}$$

where U_d (V) represents the surface potential of the droplet in volts. W_e (J) represents the stored electrostatic energy of the droplet in joules.

Assuming that the decrease in surface tension caused by the charge on the droplet is represented by $\Delta\sigma$, the corresponding change in surface energy of the droplet, ΔW_S (J), can be expressed as

$$\Delta W_\mathrm{S}=4\pi\Delta\sigma R^2. \tag{20}$$

In this case, the total energy possessed by the droplet is given by $W=W_\mathrm{e}+\Delta W_\mathrm{S}$. According to the principle of virtual work, the following can be obtained:

$$\frac{\mathrm{d}W}{\mathrm{d}R}=-\frac{Q_\mathrm{d}^2}{8\pi\varepsilon_\mathrm{r}\varepsilon_0 R^2}+8\pi\Delta\sigma R=0. \tag{21}$$

Therefore,

$$\Delta\sigma=\frac{Q_\mathrm{d}^2}{64\pi^2\varepsilon_\mathrm{r}\varepsilon_0 R^3}. \tag{22}$$

If $\sigma=\Delta\sigma$ indicates that the static pressure generated by surface tension is completely balanced by the electrostatic expansion force, the droplet will undergo deformation and fragmentation. Thus,

$$\sigma=\frac{Q_\mathrm{Cr}^2}{64\pi^2\varepsilon_\mathrm{r}\varepsilon_0 R^3}. \tag{23}$$

Here, Q_Cr represents the limit charge of the droplet and can be calculated by

$$Q_\mathrm{Cr}=8\pi\sqrt{\sigma\varepsilon_\mathrm{r}\varepsilon_0 R^3}. \tag{24}$$

According to the limit charge of the droplet, the limit charge–mass ratio C_Cr can be obtained:

$$C_{Cr}=6\sqrt{\frac{\sigma\varepsilon_\mathrm{r}\varepsilon_0}{R^3\rho_\mathrm{l}^2}}. \tag{25}$$

When the actual charge of the droplet is $Q_\mathrm{d}<Q_\mathrm{Cr}$, the droplet remains in a stable state. In this case, the effective surface tension of the droplet can be defined as follows:

$$\sigma^*=\sigma-\frac{Q_\mathrm{d}^2}{64\pi^2\varepsilon_\mathrm{r}\varepsilon_0 R^3}. \tag{26}$$

The relationship between the effective surface tension of the droplet and the actual charge-to-mass ratio (C_Z) can be expressed as follows:

$$\sigma^*=\sigma-\frac{C_\mathrm{Z}^2 R^3\rho_\mathrm{l}^2}{36\varepsilon_\mathrm{r}\varepsilon_0}. \tag{27}$$

The outlet of an internal-mix two-phase flow electrostatic nozzle is in the form of an annular liquid film. The annular liquid film at the nozzle outlet must be converted into a spherical droplet of equal volume. The volume of the annular liquid film can be calculated as follows:

$$V_\mathrm{l}=\pi(r_0^2-r_\mathrm{g}^2)L, \tag{28}$$

where V_l (m^3) represents the volume of the annular liquid film in cubic meters. L (m) represents the length of the annular liquid film in meters.

Given the lateral oscillations present on the surface of the liquid film, the edges of the annular liquid film are irregular. Therefore, measuring the length of the film directly is impractical. Therefore, a fitting calculation is necessary. After removing lens spots from the image, the image is converted into a binary image. From the top, bottom, and right directions, the first black pixel is approximated, as shown in Fig. 10. The region of interest for calculating the liquid film at the nozzle outlet is automatically cropped. Then, the total number of pixels and the number of black pixels within the rectangular region are calculated, thus allowing for the determination of the proportion of black pixels. By considering the inherent pixel value-to-actual size ratio of the image, the equivalent length of the annular liquid film, which is denoted as L'(m), is obtained.

For each operating condition, 20 images were analyzed, and their average values were obtained by considering

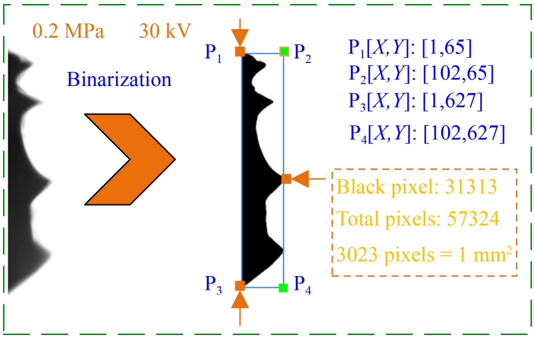

Fig. 10 Calculation scheme of equivalent length of liquid film.

different air pressures and voltages. The calculation revealed that the equivalent length of the annular liquid film, L', fluctuates between 0.264 and 0.291 mm across all operating conditions. This trend indicates that the difference in the equivalent length of the annular liquid film is not significant under different operating conditions. Furthermore, the equivalent length of the liquid film exhibits a linear relationship with the equivalent particle diameter. Therefore, an approximate value of 0.276 mm can be selected as the average value. Subsequently, the radius of the spherical droplet with an equivalent volume to the annular liquid film, which is denoted as R', can be calculated as follows:

$$R' = \sqrt[3]{0.75\pi(r_0^2 - r_g^2)L'}. \tag{29}$$

The effective surface tension of the charged annular liquid film is given by

$$\sigma^* = \sigma - \frac{C_Z^2(r_0^2 - r_g^2)L'\rho_1^2}{48\varepsilon_r\varepsilon_0}. \tag{30}$$

Based on the analysis above, the change in the potential energy of surface tension of the system before and after liquid atomization is primarily influenced by the variations in the average droplet size and the coefficient of surface tension. When the initial droplet volume is large, it possesses a relatively low potential energy of surface tension, thus having a minimal impact on the overall change in the system's potential energy of surface tension.

4.2 Change in the kinetic energy of the atomization system

The primary source of atomization energy in an internal-mixing two-phase flow nozzle is the kinetic energy provided by the compressed air in the atomization system. During the atomization process, intense interaction and energy exchange occur between the gas and liquid phases. However, this highly complex phenomenon results in a reduction of the kinetic energy of gas. The consumption of this kinetic energy can be attributed to several factors, including the increase in the kinetic energy of droplets, the viscous dissipation from droplet deformation, the increase in surface energy due to droplet breakup, and the heat carried away by droplet evaporation. In the absence of the liquid phase, the high-speed compressed gas flows out of the nozzle and enters the stationary fluid region without any restriction. When the pressure is 0.1 MPa, the Reynolds number at the nozzle outlet is higher than 5000. Moreover, the formed jet is a circular turbulent free jet, as presented in Fig. 11. The circular nozzle with a radius of r_0 generates a two-dimensional turbulent free jet that is characterized by tangential shear layers between the jet and the surrounding stagnant fluid. Intense vortex microgroups can be found at the discontinuity, which leads to the momentum exchange, mass exchange, and heat exchange between the jet and the surrounding medium. At the nozzle outlet AA′, the jet velocity is denoted as u_0, while ABCD and A′B′C′D′ represent the outer boundaries of the jet. AE and A′E are the inner boundary lines of jet. In addition, the area included in the inner boundary line is called the core area of the jet, where the velocity remains at the outlet velocity u_0 without being affected by turbulent mixing. The region between the inner and outer boundaries, ΔABE and ΔA′B′E′, is known as the mixing region of the jet. The mixing region enlarges because of the entrainment effect at the boundary, thus continuously drawing in the surrounding fluid. The core region and the mixing region constitute the initial segment of the jet. The downstream of the initial segment is the turbulent mixing region, which is referred to as the main body segment of the jet, where the jet further develops and expands its width. Furthermore, a transitional segment exists between the initial segment and the main body segment; however, this segment is relatively short and often neglected in engineering applications for simplicity [53].

Apart from viscous shear stress between layers, turbulent shear stress also occurs on the boundary of

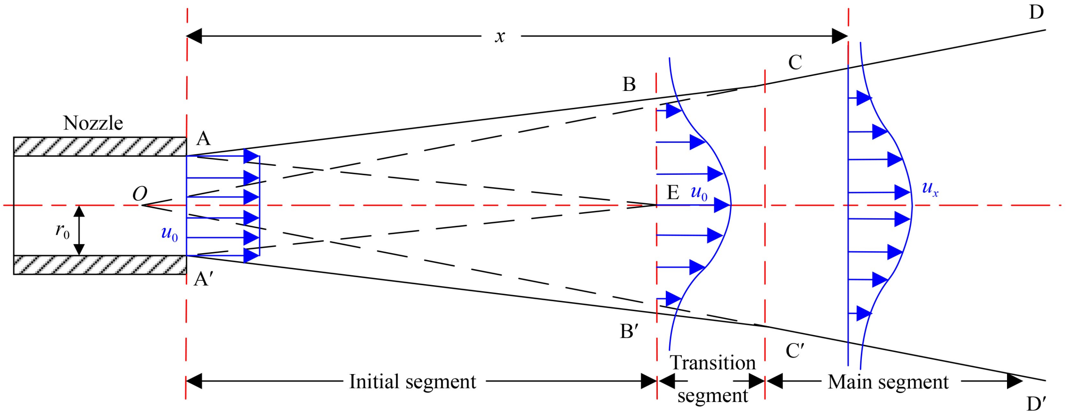

Fig. 11 Binary turbulent circular free jet.

turbulent jets because of the mass exchange and momentum transfer between adjacent layers caused by the fluctuation of turbulent particles. This is phenomenon is also called the Reynolds shear stress [54]. As shown in Fig. 12, a microliquid mass is assumed to be at point r in the flow field. Its axial pulsation velocity is u', and the radial pulsation velocity is v'. According to Prandtl's assumption, regardless of whether the microliquid mass is pulsating to the ($r + l$)-liquid layer with a higher flow rate or the ($r - l$)-liquid layer with a lower flow rate, it needs to go through a distance l' that does not collide with other microfluids. This distance is also known as the Prandtl mixing length. After the microliquid mass is pulsating to other layers, its original momentum is still mixed with the surrounding liquid phase. According to the momentum theorem and the principle of continuity, the turbulent shear stress can be obtained as $-\rho\overline{u'v'}$.

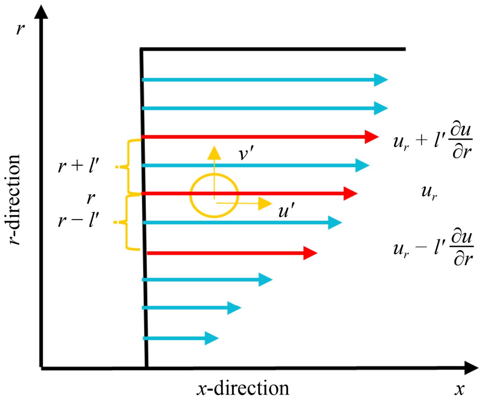

Fig. 12 Turbulent mixing length and time-averaged velocity distribution.

Given that the radial scale of the turbulent free jet is much smaller than the axial scale, the radial time-averaged velocity is much smaller than the axial time-averaged velocity. Moreover, the axial gradient of the time-averaged physical quantity is much smaller than the radial gradient. The boundary layer control equation of the circular turbulent free jet can be obtained by ignoring the small amount of magnitude comparison:

$$\frac{\partial u}{\partial t}+u\frac{\partial u}{\partial x}+v\frac{\partial u}{\partial r}=-\frac{1}{\rho}\frac{\partial p}{\partial x}+\frac{1}{\rho r}\frac{\partial r(\tau_1+\tau_2)}{\partial r}, \tag{31}$$

$$\frac{\partial (ru)}{\partial x}+\frac{\partial (rv)}{\partial r}=0, \tag{32}$$

where x represents the axial coordinate, r represents the radial coordinate, u represents the mean axial velocity, v represents the mean radial velocity, $\tau_1=\mu\frac{\partial u}{\partial r}$ represents the viscous shear stress in the jet, and $\tau_2=-\rho\overline{u'v'}$ represents the turbulent shear stress. Given that the viscous shear stress is much smaller than the turbulent shear stress in a turbulent free jet, the τ_1 term is often neglected in practical calculations. Additionally, the axial mean pressure gradient $\frac{\partial p}{\partial x}$ can be considered a small quantity and can be neglected. Therefore, for a circular, axisymmetric turbulent free jet, the simplified boundary layer governing equations along the axial direction can be expressed as follows [53,54]:

$$u\frac{\partial u}{\partial x}+v\frac{\partial u}{\partial r}=\frac{1}{\rho r}\cdot\frac{\partial (r\tau_2)}{\partial r}, \tag{33}$$

$$\frac{\partial (ru)}{\partial x}+\frac{\partial (rv)}{\partial r}=0. \tag{34}$$

The aforementioned boundary control equations are not closed. To complete them, the Tollmien solution is used along with the Prandtl turbulent shear stress relation, which can be expressed as follows:

$$\frac{\tau_2}{\rho}=l^2\left(\frac{\partial u}{\partial r}\right)^2, \tag{35}$$

where l represents the mixing length at any cross-section of the jet. A dimensional analysis reveals the following:

$$b\propto x,\ \ l\propto \alpha x, \tag{36}$$

where b represents the jet expansion width. α is the free constant, considering the self-similarity of the free jet. From this, the following can be obtained:

$$\frac{u}{u_{\mathrm{m}}}=f\left(\frac{r}{b}\right)=f\left(\frac{r}{Cx}\right)=f(\varphi), \tag{37}$$

where u_{m} represents the centerline jet velocity. C is a proportionality constant. Given the relationship $u_{\mathrm{m}}\propto 1/x$, the above equation can be written as

$$u=u_{\mathrm{m}}f(\varphi)=\frac{C_1}{x}f(\varphi), \tag{38}$$

where C_1 is a dimensional constant. By introducing the Stokes stream function ψ, and combining it with the continuity Eq. (32), the following can be obtained:

$$\psi=\int ru\mathrm{d}r=C^2x^2u_{\mathrm{m}}\int\varphi f(\varphi)\mathrm{d}\varphi=C^2C_1xF(\varphi), \tag{39}$$

where $F(\varphi)=\int\varphi f(\varphi)\mathrm{d}\varphi$. Set $F'=\frac{\mathrm{d}F}{\mathrm{d}\varphi}$, then

$$u=\frac{1}{r}\frac{\partial\psi}{\partial x}=\frac{C_1}{x}\frac{F'}{\varphi}, \tag{40}$$

$$v=-\frac{1}{r}\frac{\partial\psi}{\partial x}=\frac{CC_1}{x}(F'-F/\varphi). \tag{41}$$

Therefore, the convective term of the free jet can be expressed as

$$u\frac{\partial u}{\partial x}+v\frac{\partial u}{\partial r}=-\frac{C_1^2}{x^3}\frac{1}{\varphi}\frac{\mathrm{d}}{\mathrm{d}\varphi}\left(\frac{FF'}{\varphi}\right). \tag{42}$$

The term for turbulent shear stress in the jet is given by

$$\frac{\tau_2}{\rho}=l^2\left(\frac{\partial u}{\partial r}\right)^2=\frac{\alpha^2}{C^2}\frac{C_1^2}{x^2}\left(\frac{F''}{\varphi}-\frac{F'}{\varphi^2}\right)\left|\frac{F''}{\varphi}-\frac{F'}{\varphi^2}\right|, \tag{43}$$

$$\frac{1}{\rho r}\frac{\partial(r\tau_2)}{\partial r}=-\frac{\alpha^2}{C^3}\frac{C_1^2}{x^3}\frac{1}{\varphi}\frac{\mathrm{d}}{\mathrm{d}\varphi}\left[\frac{(F''-F'/\varphi)^2}{\varphi}\right], \tag{44}$$

where α is an arbitrary constant. As a result, let $\alpha^2 = C^3$. By substituting Eqs. (29) and (30) into the boundary control equations, the following can be obtained:

$$\frac{\mathrm{d}}{\mathrm{d}\varphi}\left(\frac{FF}{\varphi}\right)=\frac{\mathrm{d}}{\mathrm{d}\varphi}\left[\frac{(F-F/\varphi)^2}{\varphi}\right]. \tag{45}$$

After rearranging,

$$F''=F'\varphi^{-1}-\sqrt{FF'}. \tag{46}$$

The boundary conditions for the jet can be listed as follows. At the centerline of the jet, note that $r = 0$, $\varphi = 0$, $u = u_{\mathrm{m}}$, $v = 0$, $F'/\varphi = u/u_{\mathrm{m}} = 1$, $F' - F/\varphi = 0$, $F'(0) = 0$, and $F(0) = 0$. Similarly, at the far-field of the jet in the radial direction, $r = \infty$, $\varphi = \infty$, $u = 0$, $F'/\varphi = u/u_{\mathrm{m}} = 0$, and $F'(\infty) = 0$.

Using the Tollmien incremental approximation method, the numerical solution is obtained as follows:

$$b_{1/2}=1.239Cx, \tag{47}$$

where $b_{1/2}$ represents the half-jet expansion width. By substituting the Tollmien solution into the momentum equation for the jet, the following can be obtained:

$$M=\int_0^\infty \rho u^2\cdot 2\pi r\mathrm{d}r=\int_0^\infty \rho_{\mathrm{m}}^2\frac{(F')^2}{\varphi^2}\cdot 2\pi C^2x^2\varphi\mathrm{d}\varphi=\frac{\pi}{4}d^2\rho u_0^2. \tag{48}$$

After rearranging,

$$\frac{u_{\mathrm{m}}}{u_0}=\frac{1}{C\sqrt{8\beta}}\cdot\frac{d}{x}, \tag{49}$$

where $\beta=\int_0^\infty \frac{(F')^2}{\varphi}\mathrm{d}\varphi\approx 0.536$. Then,

$$\frac{u_{\mathrm{m}}}{u_0}=\frac{0.96}{C}\frac{1}{x/r_0}. \tag{50}$$

The small distance between the pole point and the nozzle exit can be neglected, and the calculation can be based on the nozzle exit as the starting point of the jet. By introducing the turbulence coefficient to analyze the variation of the single-phase jet velocity with distance, the axial velocity of the free jet can be expressed as follows:

$$u_x=\frac{0.96u_0}{\dfrac{\zeta}{r_0}+0.29}, \tag{51}$$

where u_x (m/s) represents the axial velocity at the centerline of the transverse interface at a distance x from the nozzle exit. ζ is the turbulence coefficient of the jet, which is taken as 0.007.

When the liquid phase is introduced, the interaction between the gas flow and the liquid phase leads to atomization behavior. During the transport of the charged liquid droplet group by the gas flow, an energy exchange process occurs between the gas and liquid phases at a certain distance, thus resulting in a charged two-phase flow of gas and liquid. The velocity distribution pattern of this flow is similar to that of a pure gas jet. However, with the addition of the liquid phase, the viscosity of the charged two-phase flow increases compared with that of the single-phase gas flow, thus causing changes in the velocity attenuation of the jet. For an internal-mixing two-phase flow with a circular nozzle, the following quantity relationship exists:

$$x=0.96\frac{u_0r_0\sqrt{1+S_0\Gamma_0}}{u_x\zeta\sqrt{1+0.56S_0\dfrac{u_x}{u_0}}}, \tag{52}$$

where $S_0 = m_{\mathrm{mix}}/m_{\mathrm{g}}$ is the jet density. m_{mix} (kg) is the mass of the gas-liquid mixture and m_{g} (kg) is the mass of the compressed air. Γ_0 is the initial velocity ratio, which is given by $\Gamma_0 = u_{\mathrm{l}}/u_0$, where u_{l} (m/s) is the initial velocity of the liquid at the nozzle exit.

Given that the gas-liquid velocity difference at the nozzle outlet is large, then $u_{\mathrm{l}} \ll u_0$ and $\Gamma_0 \approx 0$, which further gives an approximation of x as

$$x=0.96\frac{u_0r_0}{u_x\zeta\sqrt{1+0.56S_0\dfrac{u_x}{u_0}}}. \tag{53}$$

The velocity u_x of the gas at a fixed cross-section x in the jet can be determined based on the initial velocity of the jet, the nozzle radius, and the jet density. In this study, the initial velocity of the jet and the instantaneous liquid flow rate are known. To obtain the value of u_x, the gas mass must be calculated within a spray step. In the case of an internal-mixing two-phase flow, where the liquid film at the nozzle exit is in the form of an annular film, the accurate calculation of gas mass requires the determination of the radius of the gas core within the liquid film, r_{g}. The void fraction within the annular liquid film, which is defined as α, represents the ratio of the area occupied by the gas core to the cross-sectional area of the nozzle exit:

$$\alpha=r_{\mathrm{g}}^2/r_0^2. \tag{54}$$

In this study, a pulsed liquid supply method is employed for the two-phase flow nozzle with a duty cycle of 1:5. The instantaneous mass flow rate $\overline{m}_{\mathrm{l}}$ (kg/s) can be obtained based on the average mass flow rate m_{l}'. If the liquid velocity at the nozzle exit v_{l} (m/s) and the liquid density ρ_{l} (kg/m^3) are known, the void fraction α can be determined using the following equation, thus allowing for the calculation of the gas core radius.

$$m_{\mathrm{l}}'=\rho_{\mathrm{l}}v_{\mathrm{l}}\pi r_0^2(1-\alpha). \tag{55}$$

By considering the gas density ρ_{g} (kg/m^3), the initial velocity of the jet u_0 (m/s), and the time required for one atomization step t (s), the gas mass m_{g} can be calculated as follows:

$$m_{\mathrm{g}} = \pi\rho_{\mathrm{g}} r_{\mathrm{g}}^2 u_0 t. \tag{56}$$

The time t required for one atomization step can be determined based on the liquid mass and the instantaneous liquid flow rate. With this information, the gas energy loss value (ΔK) at a distance x from the nozzle can be obtained:

$$\Delta K = \frac{1}{2} m_{\mathrm{g}} (u_0 - u_x)^2. \tag{57}$$

As discussed above, the attenuation of kinetic energy in the atomization system is primarily influenced by the initial velocity of the gas, the gas core radius, the nozzle exit diameter, the liquid flow rate, and the distance from the nozzle exit. These factors play significant roles in determining the rate at which the kinetic energy of the system decreases.

4.3 Change in potential energy in the atomization system

In electrostatic atomization, the electrostatic nozzle can be considered a needle-shaped electrode. It forms a needle-plate configuration with the target, which results in a nonuniform and stable electric field between them. Based on the nonuniform electric field characteristics of the needle-plate electrode configuration, a long rotating ellipsoidal coordinate system (ξ,η,α) is employed, and two rotating hyperboloids are used to approximate the surfaces of the needle tip and the plate electrodes. This process allows for the determination of the potential and the maximum field strength in the needle-plate electric field [55]. In the calculation process, a mathematical model of the potential function for the standard hyperboloids is reduced to the following boundary value problem:

$$\frac{\partial(\xi^2-1)}{\partial\xi}\frac{\partial\Phi}{\partial\xi} + \frac{\partial(1-\eta^2)}{\partial\eta}\frac{\partial\Phi}{\partial\eta} + \frac{\xi^2-\eta^2}{(\xi^2-1)(1-\eta^2)}\frac{\partial^2\Phi}{\partial\alpha^2} = 0, \tag{58}$$

$$\Phi|_{\eta=0} = 0,\ \Phi|_{\eta=\eta_0} = \Phi_0, \tag{59}$$

where Φ represents the potential function in the needle-plate electrode system. The solution for Φ is given by

$$\Phi = \frac{\Phi_0}{\ln\left(\dfrac{1+\eta_0}{1-\eta_0}\right)} \ln\left(\frac{1+\eta}{1-\eta}\right). \tag{60}$$

Based on the model from Mason theory, the electric field strength at a distance x from the nozzle exit can be constructed as follows:

$$E_x = \frac{2U_0}{(R_{\mathrm{n}}+2x)\ln[(R_{\mathrm{n}}+2d)/R_{\mathrm{n}}]}, \tag{61}$$

where E_x (V/m) represents the electric field strength at a distance x from the nozzle exit. R_{n} is the curvature radius of the nozzle, which is taken as 15×10^{-6} (m).

Charged liquid droplets move downstream in the jet under the influence of gas drag and electric field forces. During the motion, the electric field works on the charged liquid droplets. The work done by the electrostatic field ΔW_{E} can be expressed as follows:

$$\Delta W_{\mathrm{E}} = Q_{\mathrm{d}}(U_0 - U_x), \tag{62}$$

where U_x represents the potential at the position where the liquid droplet is located after its motion. U_x can be expressed as follows:

$$U_x = \int \frac{2U_0}{(R_{\mathrm{n}}+2x)\ln[(R_{\mathrm{n}}+2d)/R_{\mathrm{n}}]}\mathrm{d}x. \tag{63}$$

Therefore, ΔW_{E} can be computed as follows:

$$\Delta W_{\mathrm{E}} = Q_{\mathrm{d}}\left(U_0 - \int \frac{2U_0}{(R_{\mathrm{n}}+2x)\ln[(R_{\mathrm{n}}+2d)/R_{\mathrm{n}}]}\mathrm{d}x\right). \tag{64}$$

The charge on the liquid droplets can be determined by the spray charge-to-mass ratio and the liquid mass. Therefore,

$$\Delta W_{\mathrm{E}} = m_{\mathrm{l}} C_{\mathrm{Z}} U_0 \left(1 - \frac{\ln(R_{\mathrm{n}}+2x)}{\ln[(R_{\mathrm{n}}+2d)/R_{\mathrm{n}}]}\right). \tag{65}$$

Based on the derived equation, the work done by the charged liquid droplets in a nonuniform electric field is primarily determined by the liquid mass, the charge-to-mass ratio, the nozzle voltage, the distance between electrodes, and the distance from the nozzle exit.

By substituting the surface potential energy change (ΔW_{S}) after liquid fragmentation, the loss of kinetic energy of gas (ΔK), and the work done by the electric field (ΔW_{E}) into Eq. (12), the energy distribution ratio T can be obtained as follows:

$$T = \frac{4\pi\sigma R^2(R-r)}{\dfrac{1}{2}m_{\mathrm{g}}(u_0-u_x)^2 + m_{\mathrm{l}} C_{\mathrm{Z}} U_0\left(1 - \dfrac{\ln(R_{\mathrm{n}}+2x)}{\ln[(R_{\mathrm{n}}+2d)/R_{\mathrm{n}}]}\right)}. \tag{66}$$

5 Results and analysis of the energy distribution ratio model

5.1 Determination of model input parameters

Equation (16) indicates that the radius sizes of mother droplets and daughter droplets before and after liquid breakup must be given, along with the surface tension of liquid under different charging conditions. Thus, the change value of the potential energy of surface tension before and after liquid atomization can be obtained. Given that the initial potential energy of the surface tension of the liquid is relatively small, approximating the annular liquid film as a spherical droplet introduces negligible errors in the model. The initial particle size of the mother droplet before crushing was calculated with a liquid volume of 2 mL as a fog chemical step. The microlubricant used in the study is soybean oil. Its density is 916.8 kg/m^3, and its mass is 1.8336×10^{-3} kg. Additionally, according to the principle of equal volume transformation, the annular liquid film can be approximated as a spherical droplet with a radius of 7.8172×10^{-3} m^3. The initial velocity of the gas at the nozzle outlet is measured by the flowmeter. The analysis shows that the influence of the electric field on the gas velocity is negligible. The measured gas velocities under conditions of 0.1–0.4 MPa are 38.25, 56.38, 69.40, and 79.92 m/s, respectively. The surface tension of the liquid under different voltages is determined by measuring the charge-to-mass ratio. In this study, the real charge-to-mass ratio is determined using a Faraday pail and a picoammeter. Given that the droplet sizes formed during atomization exhibit a certain distribution width rather than being uniformly distributed, the VAD of the droplets in the atomization system under different gas pressures and voltages is estimated using a Winner319 laser particle size analyzer. Specific results can be found in Section 2.3.

The analysis reveals that the charge-to-mass ratio of the liquid is independent of the distance from the measurement point to the nozzle exit. Figure 13 presents the measured real charge-to-mass ratios under different voltages and gas pressures. At the same gas pressure, the charge-to-mass ratio of the droplets increases with the voltage. This behavior can be attributed to the stronger charging capability associated with higher nozzle voltage. However, as the voltage continues to increase, the increment of the charge-to-mass ratio diminishes. This trend can be attributed to the liquid reaching its maximum charge limit, thus causing a challenge for the liquid to acquire additional charge at higher voltages. Under the same voltage, the charge-to-mass ratio of the liquid decreases with increasing gas pressure. This trend can be explained by the increase in gas velocity at the nozzle exit with high gas pressure. The energy exchange between the gas and liquid results in an increase in liquid velocity. Consequently, the contact time between the liquid and the nozzle decreases, thus leading to a reduction in the charge-to-mass ratio of the liquid. Moreover, this trend becomes pronounced with increasing gas pressure. The maximum charge-to-mass ratio obtained at a gas pressure of 0.1 MPa and a voltage of 40 kV is 0.3078 mC/kg, while the minimum charge-to-mass ratio obtained at a gas pressure of 0.4 MPa and a voltage of 20 kV is 0.1156 mC/kg.

Under different pressure and voltage conditions, the mass of the liquid (m_l) within a single atomization step can be calculated as 1.8336×10^{-3} kg based on the liquid volume and density. However, the gas mass (m_g) varies because of the changing gas core radius (r_g) within the atomization step under different pressure and voltage conditions. Equation (42) represents the velocity of the liquid film at the nozzle exit to determine the gas core radius. However, given the complex interactions among the liquid phase, gas phase, and electric field at the nozzle exit, no theoretical formula is currently available to calculate the velocity accurately. In this study, PIV, a high-speed form of photography, is employed to analyze the liquid film at the nozzle exit. Binary images are obtained by capturing images of the adjacent nozzle liquid films. The coordinate values of the first black pixel approaching from the right side of the image are recorded, along with the X-coordinate value of the rightmost black pixel from the adjacent captured image (as shown in Fig. 14). The difference in X-coordinate values between the two adjacent images represents the distance traveled by the liquid film. A time interval of 0.002 s is maintained between consecutive photos. Additionally, the pixel-to-real size ratio is used to determine the velocity of the liquid phase at the nozzle exit.

Under different nozzle gas pressure P (MPa) and voltage U (kV) conditions, 20 sets of adjacent images are analyzed and averaged to determine the average liquid phase velocity u_l at the nozzle exit, as shown in Fig. 15.

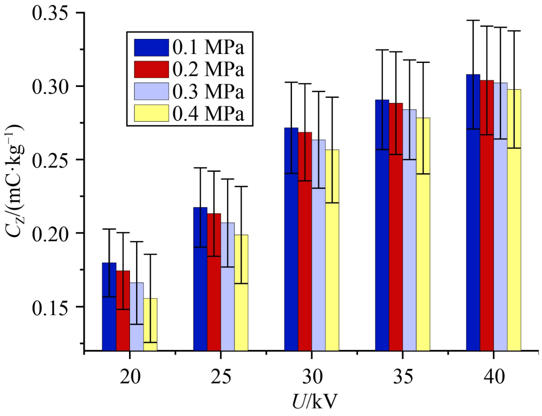

Fig. 13 Droplet charge-mass ratio under different pressure and voltage conditions.

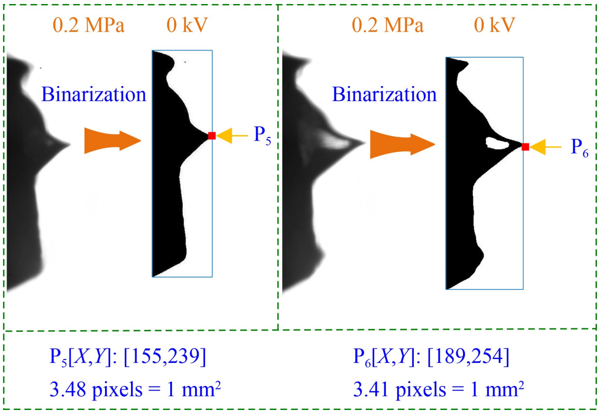

Fig. 14 Calculation scheme of liquid film velocity at nozzle outlet. Time lag = 0.004 s.

The results show that the liquid velocity increases with rising gas pressure. The rate of increase in liquid velocity is pronounced within the gas pressure range of 0.1–0.3 MPa, while the increment diminishes when the gas pressure reaches 0.4 MPa. This analysis suggests that as the gas pressure rises, the exchange of kinetic energy between the gas and liquid intensifies, thus leading to a substantial increase in liquid velocity. However, when the gas pressure reaches 0.4 MPa, the increment in liquid velocity becomes limited because of the constraints imposed by the energy exchange interface. Under the same gas pressure conditions, the liquid velocity increases with higher voltage. Compared with gas pressure, the effect of voltage on liquid velocity is comparatively minor.

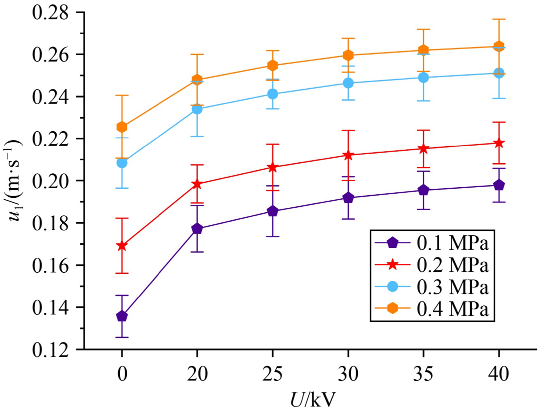

Fig. 15 Liquid velocity at nozzle outlet under different voltage and pressure conditions.

Based on the liquid volume within a single atomization step and the instantaneous flow rate of the nozzle, the time duration of the atomization step (t) can be determined. Moreover, by utilizing the atomization time, initial gas velocity, and gas core radius, the gas mass (m_g) within a single atomization step under different voltage and gas pressure conditions can be calculated, as shown in Fig. 16. The gas mass exhibits a significant increase with rising gas pressure, and the magnitude of this increase is substantial. However, the impact of voltage on the gas mass is minimal. This analysis suggests that the negligible influence of voltage is attributed to the variation in gas core radius caused by the charging effect.

Equation (57) shows that the change in the kinetic energy of gas within the atomization system can be determined by the gas mass within a single atomization step and the difference between the initial gas velocity and the velocity at the detection point. Additionally, Eq. (40) demonstrates that the velocity at the detection point depends on factors such as the distance from the nozzle to the detection point, spray density, initial gas velocity, nozzle voltage, and nozzle radius.

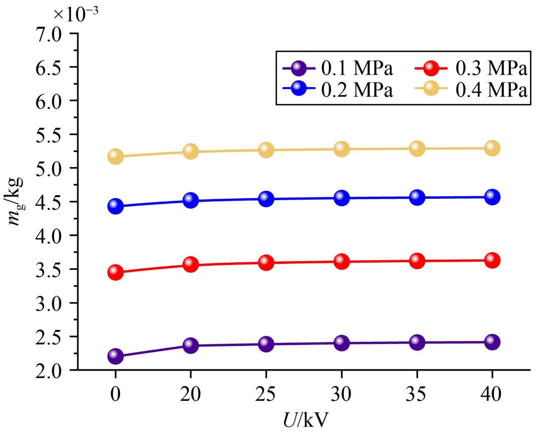

Fig. 16 Gas quality in one atomization step under different voltage and pressure conditions.

5.2 Model result analysis

I. Variation of the potential energy of surface tension of atomization system.

Based on the provided model input parameters and Eq. (16), Fig. 17 demonstrates the variation in the potential energy of the surface tension of the atomization system before and after breakup. The change in the potential energy of surface tension across different cross-sections at varying distances from the nozzle outlet aligns with the variation in gas pressure. As the spray distance and pressure increase, the change in the potential energy of surface tension also increases. This phenomenon is attributed to heightened pressure, which intensifies the energy exchange between the gas and liquid phases, thereby facilitating liquid breakage. The increase in the potential energy of surface tension remains relatively consistent among the cross-sections when the gas pressure ranges between 0.1 and 0.3 MPa. However, at a gas pressure of 0.4 MPa, the magnitude of change in the potential energy of surface tension gradually amplifies with increasing spray distance because gas energy increases with the increase of gas pressure. However, given the limitation of the atomization space, incomplete energy exchange occurs. With increasing spray distance, the atomization space expands, thus leading to a substantial enhancement in droplet breakup capability. In addition, the energy constraint point is observed between 0.3 and 0.4 MPa of gas pressure near the nozzle. Increasing the gas pressure near the nozzle further will result in a diminishing increase in the potential energy of surface tension. The atomization capability under high gas pressure can be fully demonstrated with increased spray distance and atomization space.

Furthermore, the variation of the potential energy of surface tension in the atomization system across different cross-sections exhibits distinct trends in response to voltage. Within the gas pressure range of 0.1–0.3 MPa,

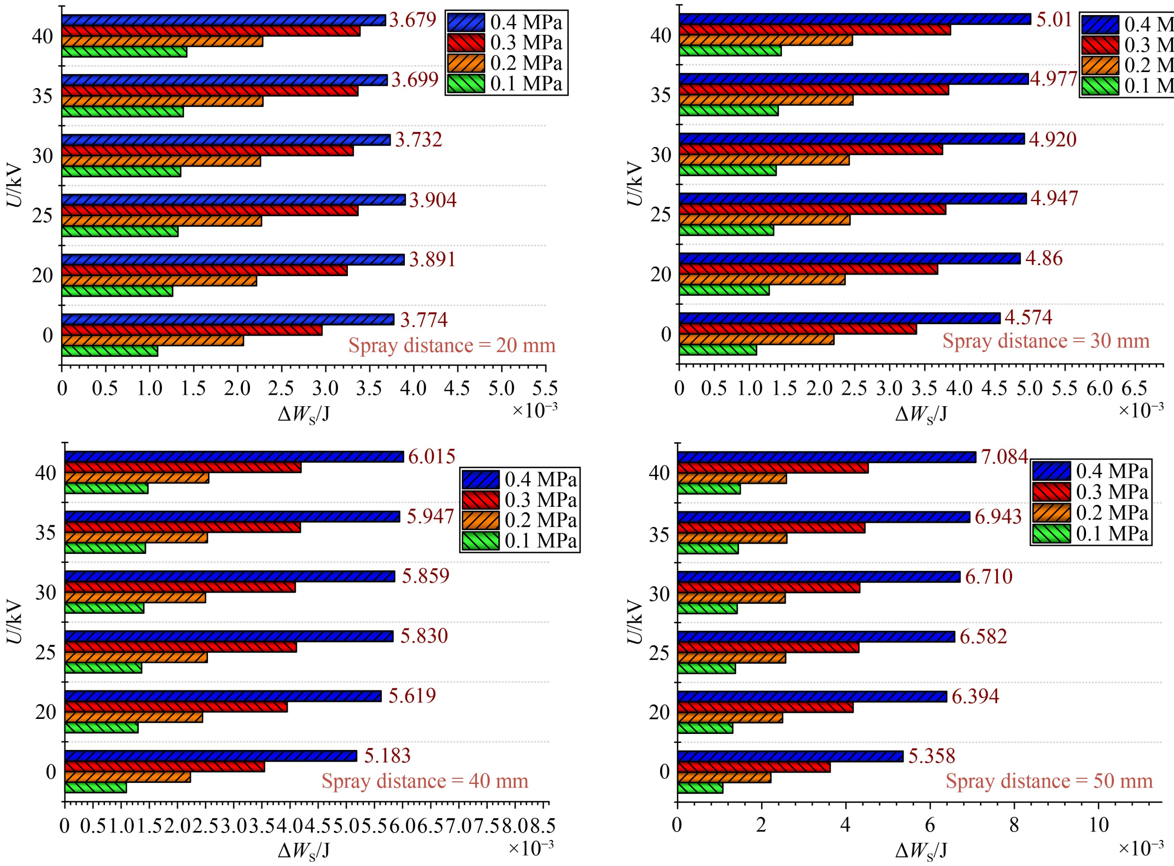

Fig. 17 Variation of the potential energy of surface tension in atomization system.

the magnitude of change in the potential energy of surface tension is greater under electrified conditions compared with nonelectrified conditions. This outcome can be attributed to the decrease in the liquid's surface tension coefficient resulting from its electrification. Moreover, the increase of the potential energy of surface tension is small with the increase of the voltage. Based on the aforementioned analysis, the energy exchange between gas and liquid is more efficient within this gas pressure range, and the influence of gas pressure on liquid breakup is more pronounced. However, this pattern undergoes a shift when the gas pressure reaches 0.4 MPa. At a distance of 20 mm from the nozzle, the variation in the potential energy of surface tension deviates from other cross-sectional positions. The change in this potential energy does not exhibit a monotonic increase with increasing voltage but rather shows an initial increase followed by a subsequent decrease. This phenomenon can be attributed to a pronounced reduction in the liquid's surface tension coefficient at high voltages. Nevertheless, given the limited space available for gas-liquid energy exchange, the exchange remains incomplete, thus resulting in this combined effect. With an increased spray distance, the space for gas-liquid energy exchange expands, thus gradually diminishing this phenomenon.

II. Change of gas kinetic energy in the atomization system.

Figure 18 presents the variation of the kinetic energy of gas in the atomization system under different conditions and at various ejection cross-sections. The impact of voltage on the loss of gas energy during the atomization process is minimal or even negligible. The trend of this loss remains consistent across different gas pressure conditions. As the spray distance increases, the gas energy loss continues to rise. However, the rate of increase shows a downward trend.

This analysis indicates that proximity to the nozzle outlet enhances gas expansion and intensifies the interactions among gas, liquid, and surrounding air, thus accelerating gas energy dissipation. As spray distance increases, the total gas energy progressively diminishes in conjunction with expanding atomization space, thereby resulting in a reduced magnitude of the loss of gas energy. Taking the example of a gas pressure of 0.4 MPa and a voltage of 40 kV, when the spray distance increases from 20 to 50 mm, the increase in the loss of gas energy is 58.18%, 23.76%, and 13.33%, respectively. Furthermore, at any cross-sectional position, the loss of gas energy exhibits a clear increasing trend with increasing gas pressure. For instance, at the 20 mm cross-section with a voltage of 0 kV, the system's gas energy

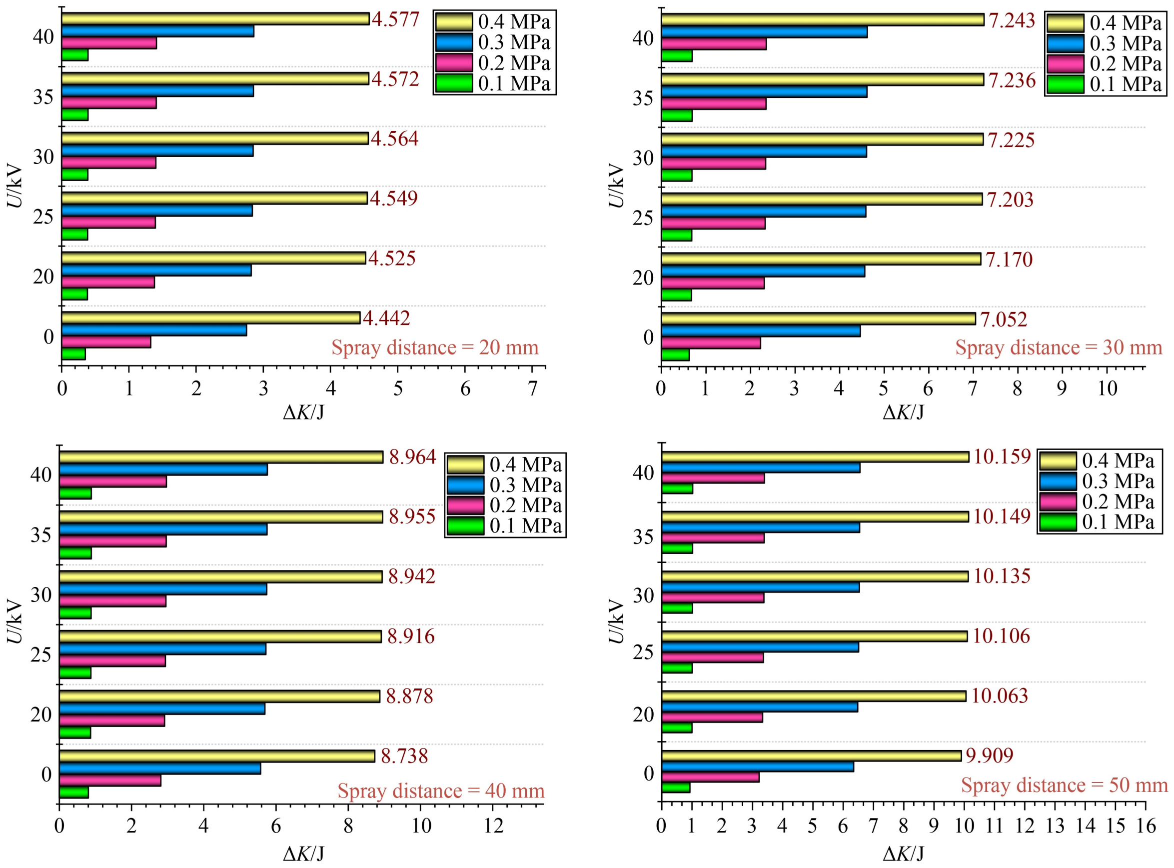

Fig. 18 Variation of gas kinetic energy in the atomization system.

losses are 0.352, 1.325, 2.752, and 4.44 J for gas pressures of 0.1, 0.2, 0.3, and 0.4 MPa, respectively.

III. Work done by the electric field force.

The movement of a charged liquid under the influence of electrostatic traction occurs in a nonuniform electric field between the nozzle and the receiving plate. During this process, the electric field force performs work, as shown in Fig. 19. The work exerted by the electric field force escalates as the cross-sectional distance expands. This phenomenon arises from the nonuniform electric field distribution between the nozzle and the receiving plate, where the electric field strength diminishes with increasing distance from the nozzle. Consequently, the rate of increase in the work done by the electric field force diminishes as the cross-sectional distance widens. Within the same cross-section, the work done by the electric field force significantly increases with the elevated nozzle voltage, which is attributed to heightened liquid charge and increased electric field strength resulting from a high nozzle voltage. However, an increase in gas pressure results in a slight decline in the work done by the electric field force. Higher gas pressure results in increased liquid velocity, thus reducing the contact time between the liquid and the charged nozzle and lowering the liquid charge. At the 50 mm cross-section, the maximum work done by the electric field force is 16.717 mJ when the voltage is 40 kV and the gas pressure is 0.1 MPa. Conversely, at the 20 mm cross-section, the minimum work done by the electric field force is 3.620 mJ when the voltage is 20 kV and the gas pressure is 0.4 MPa.

Based on the collected data concerning the variations in the potential energy of surface tension, the loss of the kinetic energy of gas, and the work done by the electric field force in the atomization system, Eq. (66) demonstrates that the energy distribution coefficient T can be obtained, as shown in Fig. 20. At the 20 mm cross-section, within the operational range of gas pressure from 0.1 MPa and voltage from 0 to 40 kV, the energy distribution coefficient falls within the range of 3.094‰ to 3.458‰. For all other operational conditions and cross-sections, the energy distribution coefficient remains below 2.06‰. The analysis suggests that at a gas pressure of 0.1 MPa, the nucleation pressure is relatively low, thus resulting in a low gas expansion rate and reduced loss of gas energy compared with other gas pressure conditions. Moreover, the low energy distribution coefficient observed at other cross-sections, in contrast to the 0.1 MPa gas pressure case, can be attributed to the fact that when the position is closer to the nozzle outlet, the energy exchange between the gas and the surrounding environment is less complete, thus leading to diminished energy losses.

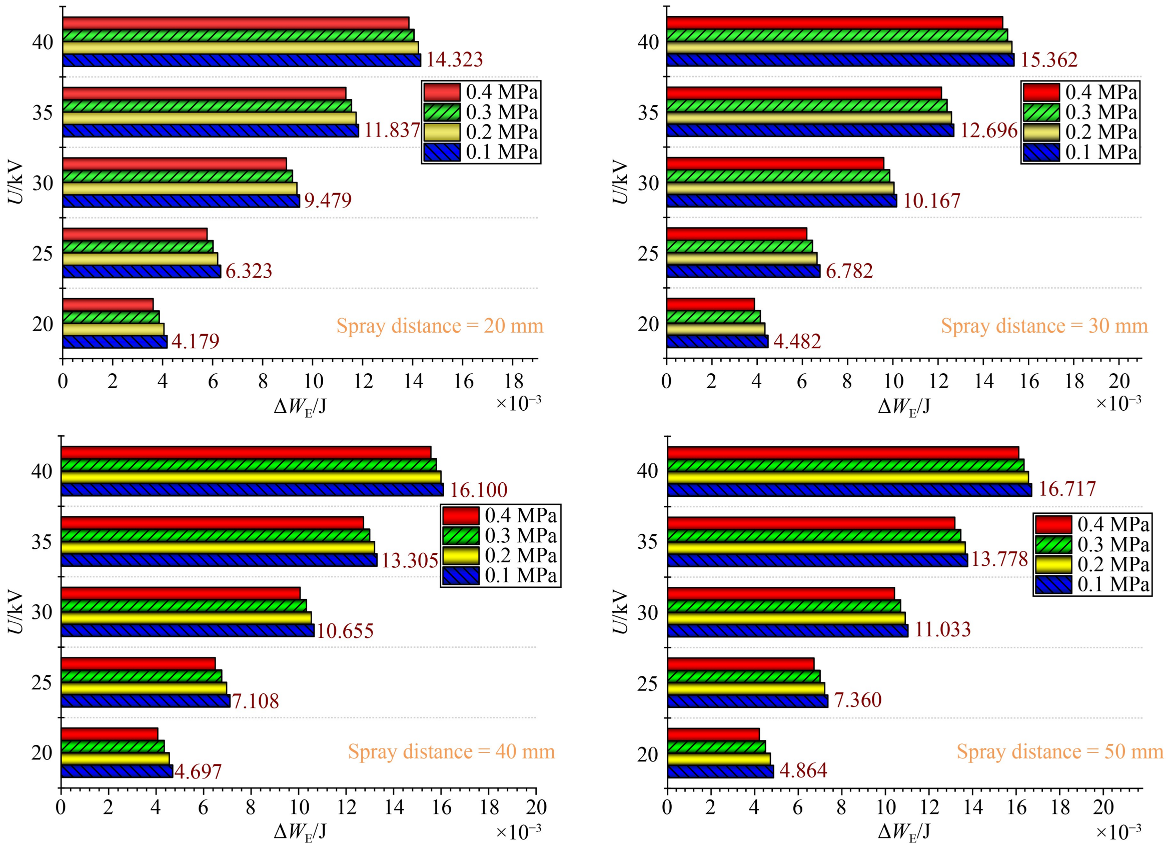

Fig. 19 Work done by electric field force in atomization process.

As shown in Fig. 20, under the same voltage condition and within a given cross-section, the energy distribution coefficient exhibits a rapid decrease with increasing system gas pressure. This trend can be attributed to the significant increase in the loss of gas energy as the gas pressure rises, as discussed in the previous analysis. Furthermore, this trend becomes pronounced as the cross-sectional distance increases because high gas pressure results in great penetration ability and intense interaction between the gas at the nozzle far end and the surrounding environment. The charged atomization system demonstrates a slightly higher energy distribution coefficient when comparing the energy distribution coefficients of the charged atomization system and the pure pneumatic atomization system under the same gas pressure condition and on the same cross-section. Although the charged atomization system incurs additional energy consumption because of the work done by the electric field force, this energy consumption is significantly smaller than the loss of gas energy. Furthermore, the decrease in the surface tension coefficient of the charged liquid enhances its susceptibility to fragmentation. Consequently, the charging of the atomization system does not increase its energy consumption. Instead, it improves the overall efficiency of the energy utilization of the system. As the gas pressure increases, the enhancing effect of voltage on the energy distribution coefficient diminishes. The substantial increase in the loss of gas energy surpasses the work done by the electric field force as the gas pressure rises. Additionally, the increase in gas pressure leads to a decrease of liquid charge.

6 Conclusions

Based on the particle size information collected at different spray distances, a dimensionless average particle size model for the fragmentation atomization of charged small liquid clusters was developed. An energy distribution ratio model for electrostatic atomization was established to investigate the energy distribution ratio during gas-assisted electrostatic atomization, as well as the effects of air velocity, voltage, and other related jet parameters on the volume-averaged droplet size. The main findings of this research work are as follows:

I. The influence of airflow field parameters and electrical field parameters on the volume-averaged droplet size was investigated based on particle size measurement experiments conducted with the EMQL nozzle at varying spray distances. Dimensional analysis was employed to establish an empirical model for the volume-averaged droplet size by incorporating factors

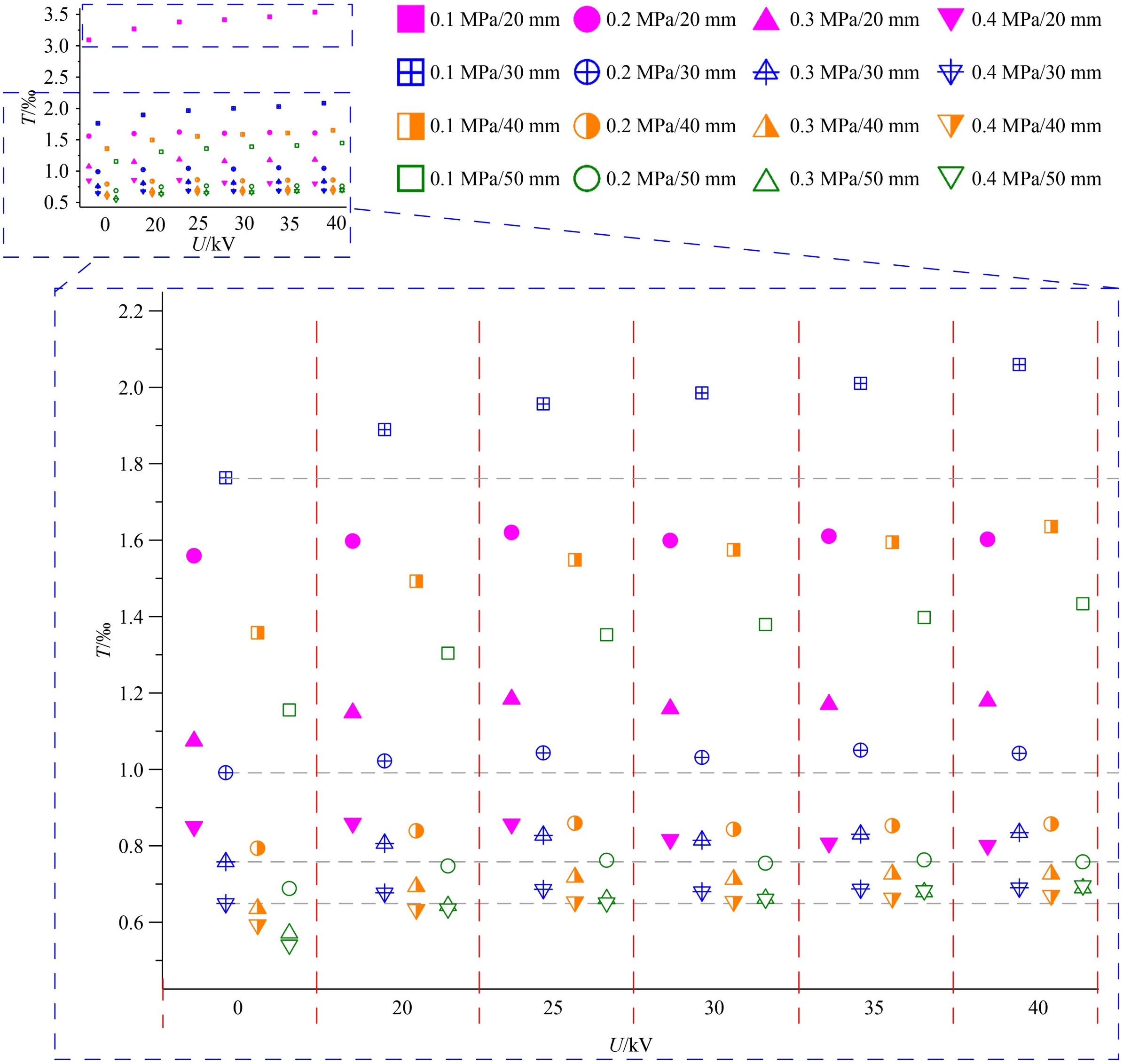

Fig. 20 Energy distribution ratio of the atomizing system.

such as initial gas velocity, nozzle voltage, and spray distance. The results revealed an inverse correlation between the volume-averaged droplet size and the Weber number, as well as the void fraction. The results indicate that the volume mean diameter of droplets exhibits negative correlations with the Weber number and void fraction as well as with the electric Euler number and the ratio of nozzle diameter to jet length. Furthermore, the influence of the airflow field on droplet size variation is more pronounced compared with the electrostatic field.

II. At air pressures ranging from 0.1 to 0.3 MPa, the potential energy of surface tension exhibited an increase with increasing air pressure, which was relatively consistent across different sections. However, at an air pressure of 0.4 MPa, a pattern emerged where the magnitude of increase in the potential energy of surface tension gradually grew with increasing spray distance. This behavior can be attributed to the decrease in the surface tension coefficient of the charged liquid, thus resulting in an enhancement of the charged potential energy of surface tension. Consequently, the potential energy of surface tension exhibited a slight increase with increasing voltage. However, at the 20 mm section under the 0.4 MPa condition, the change in the potential energy of surface tension deviated from the other conditions. In this case, the potential energy of surface tension initially increased and then decreased with increasing voltage.

III. In the atomization system, the loss of kinetic energy of gas exhibits a significant increase with air pressure and spray distance. The maximum loss of this energy is observed at the 50 mm section under an air pressure of 0.4 MPa, which reached 10.159 J at a voltage of 40 kV. The electrical field work increases with higher nozzle voltage and spray distance. At a voltage of 40 kV, the maximum electrical field work is observed at the 50 mm section, which reached 16.717 mJ under an air pressure of 0.1 MPa.

IV. The energy distribution ratio model of a gas-assisted electrostatic spray was established. The energy distribution ratio decreased significantly with the increase in air pressure and spray distance. Moreover, the coefficient of the energy distribution ratio of charged atomization was higher than that of pure pneumatic atomization. Furthermore, the energy distribution ratio in the charged atomization system is slightly higher than in pure air-assisted atomization. Specifically, at the 20 mm section, under an air pressure of 0.1 MPa and a voltage range of 0 to 40 kV, the energy distribution ratio coefficient ranged from 3.094 ‰ to 3.458 ‰. For other conditions and sections, the energy distribution ratio remained below 2.06‰.

Therefore, this study conducted a comprehensive investigation into the atomization of small liquid clusters by EMQL nozzles, thus addressing the deficiency in related research. It provides theoretical support for the further development of EMQL in enhancing the atomization characteristics of lubricants and improving the migration and permeation capabilities of droplets within the cutting zone. This study serves as a guiding force in the field by stimulating a deep contemplation on energy distribution behaviors during atomization. Thus, this work offers practical guidance for precise and controllable applications of average-sized droplets in industrial settings.

Nomenclature

Abbreviations

EMQL	Electrostatic atomization minimum quantity lubrication
MQL	Minimum quantity lubrication
PIV	Particle image velocimetry
R.S	Span values
VAD	Volumetric average diameter

Variables

A	Nozzle structure coefficient
B	Fitting index of corresponding physical quantity
b	Jet expansion width
C	Fitting index of corresponding physical quantity
C_1	Constants containing dimensions
D	Fitting index of corresponding physical quantity
d	Distance between electrostatic nozzle and target
d_0	Nozzle outlet diameter
E	Fitting index of corresponding physical quantity
E_x	Electric field intensity far from the nozzle outlet x
F_S	Nozzle diameter jet length ratio
I	Current dimension
ΔK	Loss of kinetic energy of gas
L	Length dimension
l	Mixing length of any section of jet
l'	Prandtl mixing length
M	Mass dimension
m_g	Compressed air quality
m_l	Instantaneous mass flow
m_{mix}	Mass of gas liquid mixture
$\overline{m}_l$	Average mass flow of micro lubricant
R^2	Determination coefficient
R_n	Radius of curvature of nozzle
r_0	Outlet radius of round nozzle
r_g	Radius of gas nucleus
S_0	Jet consistency
T	Time dimension
t	Time required for one atomization step
U_0	Nozzle initial voltage
U_x	Position potential of the droplet after moving
u	Axial time average velocity of microliquid mass at r point in flow field
u'	Axial fluctuating velocity of microliquid mass at r point in flow field
u_0	Initial velocity of gas at nozzle exit
u_l	Initial velocity of liquid at nozzle exit
u_m	Jet velocity on the centerline
u_x	Axial velocity of the center of the transverse section away from the exit x
v	Radial time average velocity of microliquid mass at r point in flow field
v'	Radial fluctuating velocity of microliquid mass at r point in flow field
v_l	Liquid velocity at nozzle outlet
W_{S1}	Surface potential energy of mother liquid drops before crushing
W_{S2}	Total surface potential energy of subdroplet group
ΔW_E	Work done by electric field force
ΔW_S	Variation of the potential energy of surface tension of droplet system
x	Axial distance from nozzle outlet
α	Free constant
ε_r	Relative permittivity of air
ζ	Jet turbulence coefficient
ρ_g	Gas density
ρ_l	Liquid density
σ	Surface tension coefficient

τ_1	Viscous shear stress of jet
Φ	Potential function in needle plate electrode system
Γ_0	Initial velocity ratio

Acknowledgements This study was financially supported by the Postdoctoral Science Foundation Funded Project, China (Grant No. 2023M732826), the Liaoning Provincial Science and Technology Program Project, China (Grant No. 2023JH1/10400074), the Special Fund of Taishan Scholars Project, China (Grant No. tsqn202211179), the National Natural Science Foundation of China (Grant No. 52375447), and the Liaoning Provincial Natural Science Foundation Project (Doctoral Research Start-up Project), China (Grant No. 2024-BS-239).

Conflict of Interest Changhe LI is a member of the Editorial Board of *Frontiers of Mechanical Engineering*, who was excluded from the peer review process and all editorial decisions related to the acceptance and publication of this article. Peer review was handled independently by the other editors to minimize bias.

References

1. Jia D Z, Li C H, Liu J H, Zhang Y B, Yang M, Gao T, Said Z, Sharma S. Prediction model of volume average diameter and analysis of atomization characteristics in electrostatic atomization minimum quantity lubrication. Friction, 2023, 11(11): 2107–2131
2. Chu A X, Li C H, Zhou Z M, Liu B, Zhang Y B, Yang M, Gao T, Liu M Z, Zhang N Q, Dambatta Y S, Sharma S. Nanofluids minimal quantity lubrication machining: from mechanisms to application. Lubricants, 2023, 11(10): 422
3. Gu G Q, Wang D Z, Wu S J, Zhou S, Zhang B X. Research status and prospect of ultrasonic vibration and minimum quantity lubrication processing of nickel-based alloys. Intelligent and Sustainable Manufacturing, 2024, 1(1): 10006
4. Debnath S, Reddy M M, Yi Q S. Environmental friendly cutting fluids and cooling techniques in machining: a review. Journal of Cleaner Production, 2014, 83: 33–47
5. Jia D Z, Zhang Y B, Li C H, Yang M, Gao T, Said Z, Sharma S. Lubrication-enhanced mechanisms of titanium alloy grinding using lecithin biolubricant. Tribology International, 2022, 169: 107461
6. Wang X M, Li C H, Zhang Y B, Ali H M, Sharma S, Li R Z, Yang M, Said Z, Liu X. Tribology of enhanced turning using biolubricants: a comparative assessment. Tribology International, 2022, 174: 107766
7. Vereschaka A A, Vereschaka A S, Grigoriev S N, Kirillov A K, Khaustova O U. Development and research of environmentally friendly dry technological machining system with compensation of physical function of cutting fluids. Procedia CIRP, 2013, 7: 311–316
8. Song Y X, Li C H, Zhou Z M, Liu B, Sharma S, Dambatta Y S, Zhang Y B, Yang M, Gao T, Liu M Z, Cui X, Wang X M, Xu W H, Li R Z, Wang D Z. Nanobiolubricant grinding: a comprehensive review. Advances in Manufacturing, 2024, 1–42
9. Liu D W, Li C H, Xu P M, Wang W, Zhang Y B, Yang M, Cui X, Li B K, Liu M Z, Gao T, Dambatta Y S, Qin A G. SiCp/Al composites from conventional to empowered machining: mechanisms and processability. Composite Structures, 2024, 346: 118433
10. Yang M, Ma H, Li Z H, Hao J C, Liu M Z, Cui X, Zhang Y B, Zhou Z M, Long Y Z, Li C H. Force model in electrostatic atomization minimum quantity lubrication milling Gh4169 and performance evaluation. Frontiers of Mechanical Engineering, 2024, 19(4): 28
11. Gao T, Xu P M, Wang W, Zhang Y B, Xu W H, Wang Y Q, An Q L, Li C H. Force model of ultrasonic empowered minimum quantity lubrication grinding CFRP. International Journal of Mechanical Sciences, 2024, 280: 109522
12. Qu S S, Wei C X, Yang Y Y, Yao P, Chu D K, Gong Y D, Zhao D, Zhang X P. Grinding mechanism and surface quality evaluation strategy of single crystal 4H-SiC. Tribology International, 2024, 194: 109515
13. Pillai A L, Nagao J, Awane R, Kurose R. Influences of liquid fuel atomization and flow rate fluctuations on spray combustion instabilities in a backward-facing step combustor. Combustion and Flame, 2020, 220: 337–356
14. Zhang Y, Yu N J, Tian H, Li W D, Feng H. Experimental and numerical investigations on flow field characteristics of pintle injector. Aerospace Science and Technology, 2020, 103: 105924
15. Suryaprakash R, Tomar G. Secondary breakup of drops. Journal of the Indian Institute of Science, 2019, 99(1): 77–91
16. Jain M, Prakash R S, Tomar G, Ravikrishna R V. Secondary breakup of a drop at moderate Weber numbers. Proceedings of the Royal Society A: Mathematical, Physical and Engineering Sciences, 2015, 471(2177): 20140930
17. Guildenbecher D R, López-Rivera C, Sojka P E. Secondary atomization. Experiments in Fluids, 2009, 46(3): 371–402
18. Chryssakis C, Assanis D N. A unified fuel spray breakup model for internal combustion engine applications. Atomization and Sprays, 2008, 18(5): 375–426
19. Shlegel N E, Solomatin Y S, Strizhak P A. Experimental research into the characteristics of child droplets formed due to collisions of liquid fragments in a gas. Powder Technology, 2020, 363: 122–134
20. Pham P X, Kourmatzis A, Masri A R. Local characteristics of fragments in atomizing sprays. Experimental Thermal and Fluid Science, 2018, 95: 44–51
21. Ridolfi M R, Folgarait P. Numerical modeling of secondary breakup in molten metals gas-atomization using dimensionless analysis. International Journal of Multiphase Flow, 2020, 132:

103431

22. Wei M W, Chen S Y, Sun M, Liang J, Liu C S, Wang M. Atomization simulation and preparation of 24CrNiMoY alloy steel powder using VIGA technology at high gas pressure. Powder Technology, 2020, 367: 724–739
23. Urbán A, Zaremba M, Malý M, Józsa V, Jedelský J. Droplet dynamics and size characterization of high-velocity airblast atomization. International Journal of Multiphase Flow, 2017, 95: 1–11
24. Lieber C, Koch R, Bauer H J. Spray evaporation of urea–water solution: experiments and modelling. Experimental Thermal and Fluid Science, 2020, 116: 110108
25. Shlegel N E, Tkachenko P P, Strizhak P A. Collision of water droplets with different initial temperatures. Powder Technology, 2020, 367: 820–830
26. Wang P F, Tian C, Liu R H, Wang J. Mathematical model for multivariate nonlinear prediction of SMD of X-type swirl pressure nozzles. Process Safety and Environmental Protection, 2019, 125: 228–237
27. Hu S G, Li C H, Zhou Z M, Liu B, Zhang Y B, Yang M, Li B K, Gao T, Liu M Z, Cui X, Wang X M, Xu W H, Dambatta Y S, Li R Z, Sharma S. Nanoparticle-enhanced coolants in machining: mechanism, application, and prospects. Frontiers of Mechanical Engineering, 2023, 18(4): 53
28. Urionabarrenetxea E, Avello A, Rivas A, Martín J M. Experimental study of the influence of operational and geometric variables on the powders produced by close-coupled gas atomisation. Materials & Design, 2021, 199: 109441
29. Maruda R W, Krolczyk G M, Feldshtein E, Pusavec F, Szydlowski M, Legutko S, Sobczak-Kupiec A. A study on droplets sizes, their distribution and heat exchange for minimum quantity cooling lubrication (MQCL). International Journal of Machine Tools & Manufacture, 2016, 100: 81–92
30. Park K H, Olortegui-Yume J, Yoon M C, Kwon P. A study on droplets and their distribution for minimum quantity lubrication (MQL). International Journal of Machine Tools & Manufacture, 2010, 50(9): 824–833
31. Gupta K, Laubscher R F, Davim J P, Jain N K. Recent developments in sustainable manufacturing of gears: a review. Journal of Cleaner Production, 2016, 112: 3320–3330
32. Chen M K, Zhang Y B, Liu B, Zhou Z M, Zhang N Q, Wang H H, Wang L Q. Design of intelligent and sustainable manufacturing production line for automobile wheel hub. Intelligent and Sustainable Manufacturing, 2024, 1(1): 10003
33. Krolczyk G M, Maruda R W, Krolczyk J B, Wojciechowski S, Mia M, Nieslony P, Budzik G. Ecological trends in machining as a key factor in sustainable production—a review. Journal of Cleaner Production, 2019, 218: 601–615
34. Jia D Z, Li C H, Wang S, Zhang Q. China Patent,103072084 A, 2015-09-09.
35. Sridhar R, Lakshminarayanan R, Madhaiyan K, Amutha Barathi V, Lim K H C, Ramakrishna S. Electrosprayed nanoparticles and electrospun nanofibers based on natural materials: applications in tissue regeneration, drug delivery and pharmaceuticals. Chemical Society Reviews, 2015, 44(3): 790–814
36. Yang M, Kong M, Li C H, Long Y Z, Zhang Y B, Sharma S, Li R Z, Gao T, Liu M Z, Cui X, Wang X M, Ma X, Yang Y Y. Temperature field model in surface grinding: a comparative assessment. International Journal of Extreme Manufacturing, 2023, 5(4): 042011
37. Zamani M, Prabhakaran M P, Ramakrishna S. Advances in drug delivery via electrospun and electrosprayed nanomaterials. International Journal of Nanomedicine, 2013, 8(1): 2997–3017
38. Li S J, Zhuo Z, He L J, Huang X F. Atomization characteristics of nano-Al/ethanol nanofluid fuel in electrostatic field. Fuel, 2019, 236: 811–819
39. Zheng J Q, Xu Y M, Wang Q F, He H Z. Characteristics of particle size and velocity of droplets of coal water slurry subjected to air-blast electrostatic atomization using a phase Doppler particle analyzer. Journal of Electrostatics, 2019, 98: 40–48
40. Lv T, Huang S Q, Liu E T, Ma Y L, Xu X F. Tribological and machining characteristics of an electrostatic minimum quantity lubrication (EMQL) technology using graphene nano-lubricants as cutting fluids. Journal of Manufacturing Processes, 2018, 34: 225–237
41. Hu S G, Li C H, Zhou Z M, Liu B, Zhang Y B, Yang M, Li B K, Gao T, Liu M Z, Cui X, Wang X M, Xu W H, Dambatta Y S, Li R Z, Sharma S. Nanoparticle-enhanced coolants in machining: mechanism, application, and prospects. Frontiers of Mechanical Engineering, 2023, 18(4): 53
42. Lee P H, Kim J W, Lee S W. Experimental characterization on eco-friendly micro-grinding process of titanium alloy using air flow assisted electrospray lubrication with nanofluid. Journal of Cleaner Production, 2018, 201: 452–462
43. Xu W H, Li C H, Cui X, Zhang Y B, Yang M, Gao T, Liu M Z, Wang X M, Zhou Z M, Sharma S, Dambatta Y S. Atomization mechanism and machinability evaluation with electrically charged nanolubricant grinding of GH4169. Journal of Manufacturing Processes, 2023, 106: 480–493
44. Shah P, Khanna N, Zadafiya K, Bhalodiya M, Maruda R W, Krolczyk G M. In-house development of eco-friendly lubrication techniques (EMQL, Nanoparticles+EMQL and EL) for improving machining performance of 15–5 PHSS. Tribology International, 2020, 151: 106476
45. Xu W H, Li C H, Zhang Y B, Yang M, Zhou Z M, Chen Y, Liu B, Zhang N Q, Xu X F. Research progress and application of electrostatic atomization minimum quantity lubrication. Journal of Mechanical Engineering, 2023, 59(7): 110–138
46. Airao J, Khanna N, Nirala C K. Tool wear reduction in machining Inconel 718 by using novel sustainable cryo-lubrication techniques. Tribology International, 2022, 175: 107813
47. Mia M, Dey P R, Hossain M S, Arafat M T, Asaduzzaman M, Ullah M S, Zobaer S T. Taguchi S/N based optimization of machining parameters for surface roughness, tool wear, and material removal rate in hard turning under MQL cutting condition. Measurement, 2018, 122: 380–391
48. Sultana N, Dhar N R. A critical review on the progress of MQL in machining hardened steels. Advances in Materials and Processing Technologies, 2022, 8(4): 3834–3858
49. Torabi E, Talebi K, Pourbabaee A A, Homayoonzadeh M, Ghamari M J, Ebrahimi S, Faridy N. Optimizing the QuEChERS method for efficient monitoring of fipronil, thiobencarb, and cartap

residues in paddy soils with varying properties. Environmental Monitoring and Assessment, 2024, 196(2): 125

50. Faridy N, Torabi E, Pourbabaee A A, Osdaghi E, Talebi K. Efficacy of novel bacterial consortia in degrading fipronil and thiobencarb in paddy soil: a survey for community structure and metabolic pathways. Frontiers in Microbiology, 2024, 15: 1366951
51. Naik D N S, Sharma V. An anomalous effect of steady and unsteady impingement jets on heat transfer coefficient and gradient microstructure in the machining of Ti-3Al-2.5V alloy. Journal of Manufacturing Processes, 2024, 114: 136–155
52. Wang X Y. The research and application of charged atomization. Dissertation for the Doctoral Degree. Zhenjiang: Jiangsu University, 2008 (in Chinese)
53. Liu P Q. Free Turbulent Jet Theory. Beijing: Beihang University Press, 2008, 89–131 (in Chinese)
54. Ping J. Theoretical Basis and Application of Jet Flow. Beijing: Astronautical Press, 1995, 50–100 (in Chinese)
55. Zhang K, Sun H M. Suitability analysis on needle plate electrode field strength based on mason calculation. Northeast Electric Power Technology, 2016, 37(6): 27–34 (in Chinese)